Physica B 738 (2026) 418810

Contents lists available at ScienceDirect

Physica B: Condensed Matter

journal homepage: www.elsevier.com/locate/physb

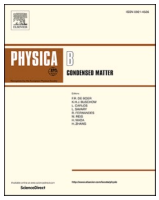

Shielding efficiency of iron doped tincal: A first-principles study

I.P. Duru [a], E. Ozugurlu [b,*], L. Arda [c]

[a] Istanbul Gedik University, Medical Imaging Program, Istanbul, Türkiye
[b] Istanbul Technical University, Faculty of Science and Letters, Department of Mathematics, Istanbul, Türkiye
[c] Bahcesehir University, Faculty of Engineering and Natural Sciences, Department of Mechatronic Engineering, Besiktas, Istanbul, Türkiye

ARTICLE INFO

Keywords:
Tincal
Dielectric function
GGA/PBESol
Shielding efficiency
Antiferromagnetism

ABSTRACT

The idea of shielding has been popular for decades as a way to reduce unwanted radiation in a variety of applications, especially in the areas of security and health. Fe-doped tincal nanoparticles were examined in this article as a possible option for this use. Density functional theory (DFT) was used to calculate the dielectric function of Fe-doped tincal and shielding efficiency (SE). Fe-doped tincal structures were subjected to geometry optimization through the substitution of Fe at particular boron sites. After determining the formation energy to evaluate stability, the optical characteristics were calculated. The process was repeated for collinearly ordered ferromagnetic (FM) and antiferromagnetic (AFM) states. Considered structures obeyed the AFM state. On the other hand, low conductivity is indicated by the Fermi level electronic density of states (DOS). While bare tincal has a large indirect band gap (~5eV), the band gap was almost nonexistent in both doped examples. The electromagnetic shielding efficiency ratings were determined to be extremely poor for all setups. Except for the low-frequency band, no discernible variations in SE were found between various configurations and photon polarizations. Significant variations were found for interactions with low-energy photons, especially in the ultraviolet spectrum.

1. Introduction

Electromagnetic shielding is becoming more and more necessary as electromagnetic waves proliferate in consumer, commercial, and industrial applications. This is because of a new type of pollution that can harm living things and cause electronic devices to malfunction. It is commonly referred to as electromagnetic interference (EMI) or radio frequency interference (RFI) [1]. The creation of safe zones requires the development of protective shielding materials in order to lessen these impacts. Such shielded environments are designed to be devoid of particular electromagnetic wave ranges in laboratory settings, removing outside interference and facilitating accurate measurements. This requirement has prompted research into a range of armoring materials that are expected to be appropriate for a variety of uses [2,3]. Due to their exceptional efficiency, iron boride (FeB) materials show great promise for shielding against electromagnetic interference (EMI) [4]. Fe-based compounds and carbonyl iron have attracted a lot of interest for use in electronics, medicine, water treatment, catalysis, and particularly EMI shielding because of their diverse range of properties, including their magnetic qualities. Additionally, Sing et al. showed that covering porous particles with conductive materials can improve their shielding effectiveness [5].

Araz used the Nicholson–Ross–Weir (NRW) method in 2018 to determine the shielding efficacy of a Fe-doped barium compound [6]. The electrical and electromagnetic shielding capabilities of hexagonal boron nitride nanoparticles reinforced in polyvinylidene fluoride nanocomposite films were examined by Sankaran et al. These composites attained a shielding effectiveness (SE) of 55 dB in the X-band frequency range (8-12 GHz), which is 20 dB higher than that of bilayer carbon nanotube films (CNTFs) [7]. Separately, the presence of an embedded GaInSn liquid metal (LM) layer was found to greatly boost the EMI shielding performance of CNTFs [8]. In a different method, it was discovered that adding fly ash (which contains 5.6%, 15.9%, and 24.3% Fe_2O_3, added separately and in combination) and graphite powder, and several kinds of carbon fiber to Portland cement paste effectively shielded against electromagnetic interference. Increasing the thickness of the material further improved this shielding effect [2].

Magnetic metals and their alloys (Fe, FeNi, FeCo) have notably high permeability. On the other hand, high conductivity precipitates eddy current losses that cause low permeability at low frequencies (in the

* Corresponding author.
E-mail address: ozugurlue@itu.edu.tr (E. Ozugurlu).

https://doi.org/10.1016/j.physb.2026.418810
Received 1 November 2025; Received in revised form 7 May 2026; Accepted 11 May 2026
Available online 12 May 2026

MHz range). The researchers focused on nano/micro-scaled materials to reduce eddy current losses. Besides the thickness, the coating on the surface of the Fe component also changes the microwave absorption properties. This can be attributed to the increasing EM wave size resonance with increasing coating thickness [9].

Because of its nanoscale characteristics, which are absent from bulk structures, such as porosity and a high magnetic moment, including superparamagnetic behavior, Fe-based nanostructure design has significantly increased in recent years. The most common types of iron are ferrite (Fe2O3), magnetite (Fe3O4), iron oxides (Würzite-FeO), and iron hydroxide (FeOOH). Although the fabrication of a magnetic iron nanostructure is quite difficult, it is possible to prepare Fe nanostructures using ball milling, DC arc plasma, and sputtering methods. These are nanolayers, nanoparticles, and core@shell structures. The oxide shells not only prevent the oxidation of Fe in contact with air but also inhibit the pre-reflections observed in pure Fe layers, which allow negligible microwave absorption due to the conductivity of Fe elements (σ∼107S/cm). Dendrite-like microstructures possess higher saturation magnetization than bulk structures. The microwave absorption properties of Fe fractal microstructures are admirable due to surface defects and large surface area [9–11]. In addition, iron can be produced in various shapes, sizes, and dimensions, such as nanowires, nanoparticles, nanorods, nanotubes, hollow fibers, microspheres, and fractal-like microstructures that increase reflection loss but do not change the average conductivity [12].

This article confidently focuses on the shielding efficiency of Fe-doped tincal (Na4B8O14.20H2O) nanoparticles. It is the first attempt, according to our best knowledge. Hence, structural, electrical, magnetic, and optical properties are examined with a broad photon energy range by ab-initio calculations. We limited the photon energy to IR, VR, and UV. Section 2 elaborates on the procedure followed in this study by introducing the considered material. The findings are explicitly given, and the results are discussed in Section 3.

2. Materials and methods

2.1. Structural properties and formation energy

The tincal unit cell given has a P3221 space group in the trigonal crystal system with lattice parameters a = 8.012 Å, b = 8.012 Å, and c = 14.448 Å and plane angles α = 115.75°, β = 115.75°, and γ = 83.71° as shown in Table 1. VESTA [13] is used to illustrate the unit cell of tincal, and Fe as given in Figs. 1 and 2, respectively. Fe is in the m3m point group in the cubic crystal system. The Generalized Gradient Approximation (GGA) in Perdew-Burke-Ernzerhöf for solids (PBESol) [14] scheme is chosen with Koelling-Harmon relativistic correction and a cut-off plane-wave basis set of 517 eV for tincal crystal and 300 eV for Fe (bcc). SCF tolerance is set to 1.0E-6 eV/atom while maximum force, maximum stress, and maximum displacement tolerances are 0.03 eV/Å, 0.05 GPa, and 1.0E-3 Å. The CASTEP code is used during calculations [15].

The DFT scheme's convergence requirements must be carefully chosen because they are frequently not universal. Fundamental physical characteristics such as orbital hybridization, direct or indirect exchange interactions, charge transfer, and spin orientations are all governed by bond lengths and angles. Moreover, by dividing the energy levels into t_{2g} and e_g subsets, crystal field effects can raise degeneracies, especially in the d-orbitals of transition elements.

Table 1
Tincal and Fe lattice parameters, unit cell angles, and unit cell volume.

	Lattice parameters (Å)	Unit cell angles (°)
Tincal	a = 8.012	α = 115.752
	b = 8.012	β = 115.752
	c = 14.448	γ = 83.710
Fe (bcc)	a = 2.482	α = 109.471
	b = 2.482	β = 109.471
	c = 2.482	γ = 109.471

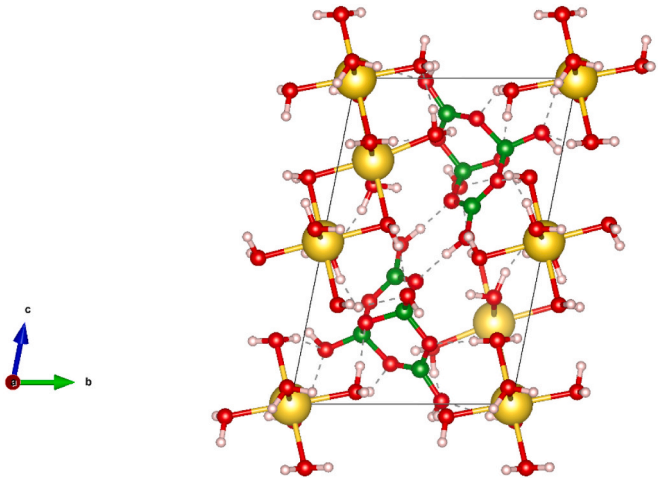

Fig. 1. In the tincal unit cell structure in the b-c plane, yellow-colored spheres represent sodium (Na), green-colored spheres represent boron (B), red-colored spheres represent oxygen (O), and transparent spheres represent hydrogen (H) atoms.

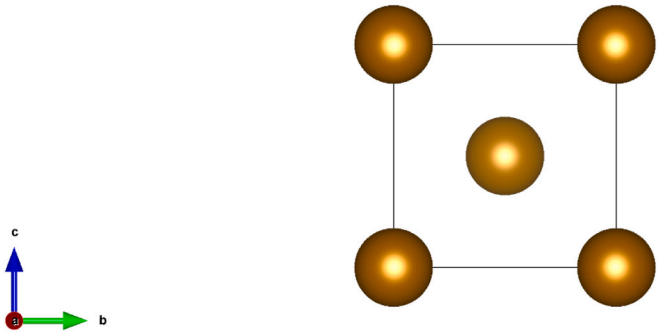

Fig. 2. The unit cell of Fe.

Fig. 2 shows the unit cell of bcc iron. The favored magnetic order is FM, and the magnetic moment of the iron atom in the FM arrangement was calculated as 2.3 μB. The formation of the structures considered is determined theoretically by calculating the formation energies. The band structures and DOS plots are revealed in the case of spin-polarized Fe ions for parallel (majority spin channels) and anti-parallel spins (minority spin channels). The bandgap is revealed by the valence band maximum (VBM) and the conduction band minimum (CBM). The exchange coupling value ($J_{Fe\text{-}Fe}$) is an easy way to determine the preferred magnetic state that the material obeys. It is related to the difference in the ground state energies between AFM and FM states.

The authors focus on the dielectric function (see Equation (1)) to figure out the optical properties and shielding efficiency. The real and imaginary parts of the dielectric function are calculated by Equation (2) and Equation (3), respectively.

$$\varepsilon(\omega) = \varepsilon_1(\omega) + i\varepsilon_2(\omega) \tag{1}$$

$$\varepsilon_1(\omega) = 1 + \frac{2}{\pi} p \int_0^{\infty} \frac{\varepsilon_2(\omega')\omega'^{\varepsilon_2}}{\omega'^2 - \omega^2} d\omega' \tag{2}$$

$$\varepsilon_2(\omega) = \left(\frac{h^2 e^2}{\pi m^2 \omega^2}\right) \sum_{C,V} \int d^3k \langle V_k | p^a | C_k \rangle \langle V_k | p^b | C_k \rangle x \delta\left(\varepsilon_{C_k} - \varepsilon_{V_k} - \omega\right) \tag{3}$$

Here, $\boldsymbol{k}$ is the momentum vector; $\boldsymbol{p}$ represents the momentum matrix

components between the a and b bands. Valence and conduction bands are indicated via $\boldsymbol{V_k}$ and $\boldsymbol{C_k}$, respectively. $\varepsilon_1(\omega)$ gives strong clues about the amount of light stopped by the material, and $\varepsilon_2(\omega)$ is the quantity of how much energy is absorbed. The absorption and reflectivity of the material, which are related to the dielectric function, are given by Equation (4) and Equation (5), where $\boldsymbol{n(\omega)} = \left[\frac{\sqrt{\varepsilon_1{}^2(\omega)+\varepsilon_2{}^2(\omega)}+\varepsilon_1(\omega)}{2}\right]^{\frac{1}{2}}$ and $\boldsymbol{k(\omega)} = \left[\frac{\sqrt{\varepsilon_1{}^2(\omega)+\varepsilon_2{}^2(\omega)}-\varepsilon_1(\omega)}{2}\right]^{\frac{1}{2}}$.

$$\alpha(\omega)=\frac{\omega\sqrt{2}}{c}\left[\sqrt{\varepsilon_1{}^2(\omega)+\varepsilon_2{}^2(\omega)}-\varepsilon_1(\omega)\right]^{\frac{1}{2}} \tag{4}$$

$$R(\omega)=\frac{(n(\omega)-1)^2+k^2(\omega)}{(n(\omega)+1)^2+k^2(\omega)} \tag{5}$$

Besides, the absorption shielding efficiency (SE_A) and the reflection shielding efficiency (SE_R) jointly form the total shielding efficiency when internal reflections are neglected. They can be obtained via absorption and reflectivity as introduced in Equation (6) and Equation (7), where $SE_T = SE_A + SE_R$.

$$SE_A(dB) = -10\,log\left(\frac{1-R}{T}\right) \tag{6}$$

$$SE_R(dB) = -10\,log\left(\frac{1}{1-R}\right) \tag{7}$$

In Section 3, the results of the electronic and optical properties of bare tincal will be first discussed. Afterward, the influence of iron doping will be handled. For each case, the formation energies are calculated, and magnetic features are sociably revealed.

3. Results & discussion

3.1. Bare tincal: A summary

The geometric optimizations of tincal and iron are performed. Then, the ground state energies are calculated, and the bandgap, state densities (DOS), and dielectric functions are obtained to gradually reveal the optical properties. Overlapping of electron integrals in atomic orbitals and hybridizations, electron transport, and direct/indirect magnetic interaction energy are directly related to structural properties. VBM and CBM are mediators to interpret the band structure. The band structure of the tincal crystal is shown in Fig. 3. The bandgap value is 5.063 eV and indirect. That is, VBM(Z) and CBM (G) are at different momentum values.

Total DOS and partial DOS of bare tincal are shown in Figs. 4 and 5, respectively. The energy units are in terms of eV. The influence of s-orbitals on electronic states around the Fermi level is lower than that of p-orbitals. The s-orbital electrons in the low-energy region (between −20 eV and −15 eV) of the valence band do not contribute as much as the p-orbital electrons. The conduction band region shows a quite similar picture. It is also necessary to interpret the atomic contributions to DOS (Fig. 5).

The influence of Sodium (Na), hydrogen (H), and boron (B) atoms on the electronic distribution at the Fermi level is lower than that of oxygen (O) atoms. Besides, though conduction band energies are diligently affected by all atoms, hydrogen dominates between 8 eV and 14 eV. Oxygen and sodium peaks at valence band depths are close to −18 eV and −21 eV, respectively. The peak around the Fermi level belongs to oxygen. The presence of oxygen in crystal structures is notable. Therefore, while evaluating the electronic properties of the tincal crystal, the closest neighbor atomic bond numbers of the oxygen, the bond lengths, and even the oxygen defects in the crystal lattice also affect the

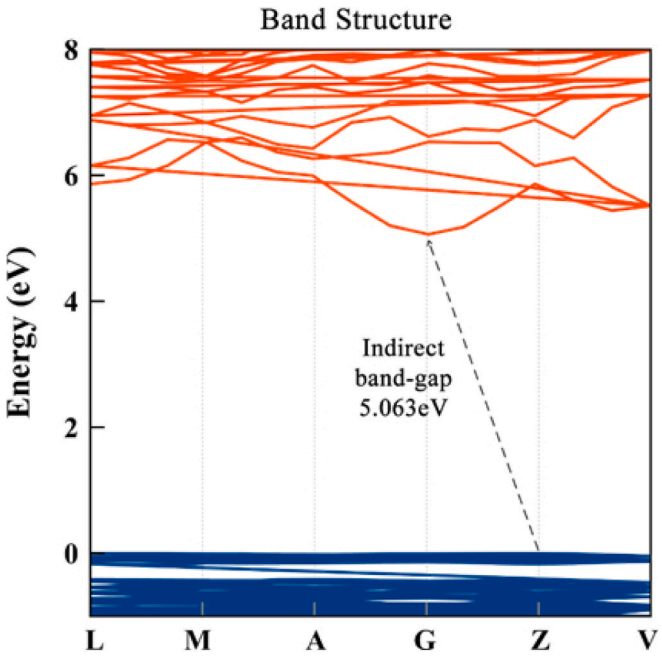

Fig. 3. Band structure and bandgap of bare tincal: Blue and orange lines represent the valence and conduction band regions, respectively.

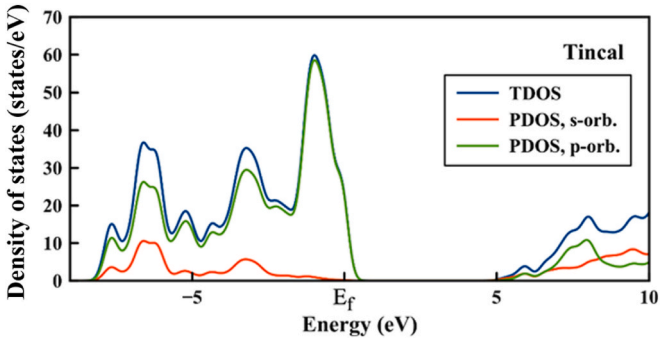

Fig. 4. The total, s-orbital, and p-orbital DOS are represented by blue, orange, and green lines, respectively.

mentioned electronic properties.

The real part underlines the material's ability to store electrical energy, introducing electronic polarizability and its refractive index, while the imaginary part incorporates the material's energy loss or light absorption. The dielectric function of bare tincal is given in Fig. 6. The imaginary part of the dielectric function takes values close to zero for photon energies less than 5 eV. The imaginary part is only active between 5 and 25 eV. Hence, the absorption of photons can be mentioned for these photon energies, and the highest absorption is for the peak at ~17 eV. On the contrary, the real part oversees low-energy photons. As the photon energy increases to ~7.5 eV, the value of the real part of the dielectric function increases and peaks at ~8 eV. The real part exhibits a decreasing trend between 8 eV and 20 eV and seems to vanish for 20 eV photons. Intriguingly, it restarts to increase and does not fluctuate under photon energies higher than 30eV. Consequently, tincal can store a respectable amount of electrical energy at lower photon energies. 8eV photons lead to the maximum stored energy (see Fig. 7).

3.2. Iron-doped tincal: Dealing with the guest effect

The chemical formula of tincal turns into $Na4(B_{1-x}Fe_x)_8O14.20H2O$ (x = 0.5, 0.25) when Fe doping takes place. B1+B2 and B1/B2

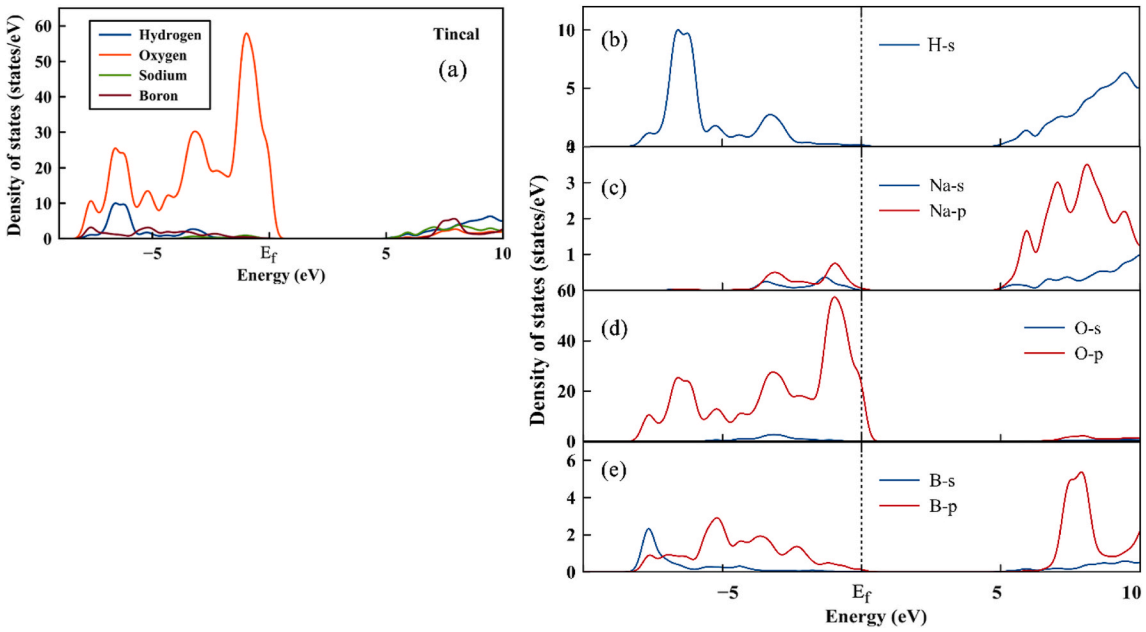

Fig. 5. (a) Atomic contributions to DOS: Na, B, H, and O atoms are represented by greenish, reddish, blue, and orange lines (b-e) atomic orbital contributions to DOS: blue line represents s-orbital while p-orbitals are reddish.

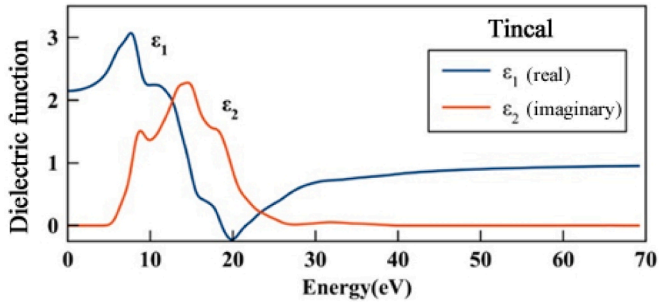

Fig. 6. The dielectric function of tincal (red solid line represents the imaginary, the blue solid line represents the real part).

configurations can be represented by the above-mentioned formula for x = 0.5 and x = 0.25, respectively. The chemical compositions wt% are Na9.97B4.69Fe24.21O58.95H2.18 for B1+B2, and Na11.04B7.79-Fe13.41O65.33H2.42 for B1/B2.

The formation energies are calculated via Equation (8) and Equation (9); thus, the most favorable site that Fe would occupy is determined. Here, n_x (x = Fe, Na, B, O, and H) indicates the number of atoms in the unit cell. These numbers vary for the different types of atoms that iron (Fe) displaces.

$$E_{for} = \frac{E_{tincal/Fe} - n_{Fe} \times E_{Fe} - n_{Na} \times E_{Na} - n_B \times E_B - n_O \times E_O - n_H \times E_H}{m} \tag{8}$$

$$m = n_{Fe} + n_{Na} + n_B + n_O + n_H \tag{9}$$

Table 2 includes the Fe-Fe exchange energies, $J_{Fe\text{-}Fe}$ obtained from ΔE of the ground state energies of each magnetic phase, magnetic moments, and formation energies for each AFM and FM case. Although the lowest energies occur in the AFM phases, the energies of the same configurations are close to each other. Tincal(B1+B2) is the most likely stable structure. The magnetic behavior of the system may be a result of the hybridization of orbitals when the guest is integrated into the pristine host material; herewith, the bond length of the nearby atom/site dihedral angle, and the type of atom considering nearest neighbors. Besides, note that superexchange, double exchange, and RKKY may also appear. The magnetic moments of iron in Tincal(B1) and Tincal(B2) configurations are calculated as 2.93 and 2.01 μB, respectively. Additionally, the formation energies and exchange energies are very close to each other. Tincal(B1+B2) is simply an association of the Tincal(B1) and Tincal(B2) cases. The average and individual moments of two boron atoms are increased proportionally to the augmented doping concentration of Fe over B. This can originate from the aggregated irons as the nearest neighbors. The exchange energies of Tincal(B1), Tincal(B2), and Tincal(B1+B2) configurations are calculated as −2.99935977 eV, −2.99676511 eV, and −0.45938324 eV, respectively. Tincal(B1) and Tincal(B2) show stronger AFM than the rest. Since AFM phases are most probable to be formed and stable, the optical properties and shielding efficiencies of AFM states are discussed in detail.

The spin density of AFM states was extracted from the DOS results and plotted on the considered configurations' atomic positions (Figs. 8 and 9). The spin values were initially assigned to Fe atoms. Yellow and blue indicate negative and positive values, respectively. Energy calculations result in an interaction between Fe-O atoms, especially the nearest Fe-O couples. The spin density distribution shows alternating positive and negative lobes localized on neighboring Fe atoms, confirming the AFM ground state. In contrast, uniform positive spin density localized on all Fe sites should be observed for FM ordering [16–18].

Comparing integrated spin densities and integrated |spin densities| jointly provides trustworthy information about the magnetic phase. Briefly, it is said to be either FM/FiM or AFM. Integrated spin densities are expected to vanish in AFM phases. The FM case requires almost the same or close values of integrated spin density and integrated |spin density|. If the integrated spin density is quite higher than zero, even if it is not so close to the integrated |spin density|, the magnetic phase is FiM. According to Table 3, B1, B2, and B1+B2 obeyed the abovementioned criteria for both AFM and FM orders.

Supporting integrated spin densities, the DOS plot of AFM and FM phases, majority and minority spin channels, shows the eV/electrons that have been procured for a certain interval of energies. One needs to focus Fermi level to attentively explain the origin of the magnetic phase. In AFM order, spin-up and spin-down symmetry should exist, especially along the Fermi level. Figs. 10(a)–Figs. 11(a) and 12(a) show the spin channel symmetry supporting integrated spin density. Moreover, DOS of

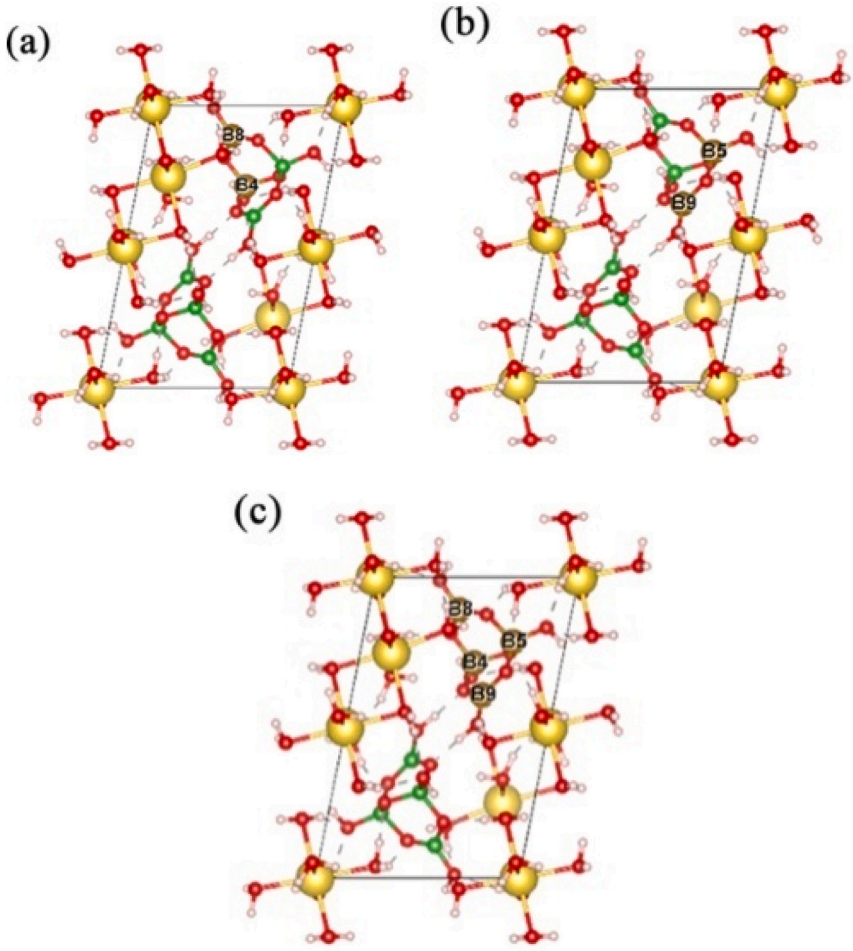

Fig. 7. Iron atoms interchange (a) B1 (atoms no. B4 and B8), (b) B2 (atoms no. B5 and B9), and (c) B1+B2 (atoms no. B4, B8, B5, and B9) in the pristine tincal unit cell. Yellow, red, green, and light pink represent Na, O, B, and H atoms, respectively, where the golden color belongs to the iron atom to illustrate the doping process.

Table 2
Formation energies (E_{for}), average magnetic moment, and exchange energies (ΔE) for the considered configurations. Note that the formation energy of Tincal is −4.46328eV.

	E_{for} (eV)		Average magnetic moment (μ_B)		ΔE (eV)
	FM	AFM	FM	AFM	
Tincal (B1)	−4.06728	−4.10216	2.47	0	−2.99936
Tincal (B2)	−4.06728	−4.10213	2.47	0	−2.99676
Tincal (B1+B2)	−4.25671	−4.26205	3.46	0	−0.45938

Fe-d and O-p were dominant along Fermi level when compared others. Fig. 10(b–g), Fig. 11(b–g), and Fig. 12(b–g) illustrated the PDOS of AFM B1, B2, and B1+B2. It is usual for FM interacted mediated by p-d hybridization. The majority and minority spin channels differ at (and around) the Fermi level; thus, unpaired electrons exist, provoking FM behavior. B1+B2 enhanced Fe-d along Fermi level due to extra Fe atoms in the unit cell. Na-p orbital strongly enriched the valence band at lower energies. In B1+B2 case, it was slightly shifted deeper. Almost all constitutents contributed to conduction band nearly the same despite Fe-d. It enhance DOS along Fermi level vanishing valence and conduction band gap. d-orbital resolved PDOS of spin-up Fe and spin-down Fe atoms were illustrated in Fig. 10(c–d), Fig. 11(c–d), and Fig. 12(c–d) in which the spin symmetry was broken for each spin-up and spin-down Fe atoms in spite of an expected symmetrical TDOS [19].

Fig. 13 illustrates the polarization direction of the photon that interacts with the Fe-doped tincal unit cell. The real part of the dielectric function, ε_1, is associated with the material's light dispersion, indicating how the speed of light changes within the material based on frequency. It specifically impacts the refractive index, illustrating the material's capacity to retain energy from an electric field without losing it. Understanding optical absorption and losses within a material is significantly aided by recognizing the importance of the imaginary part of the dielectric function, denoted as ε_2. It accounts for the dissipative component of the dielectric response, illustrating the amount of energy absorbed by the material as it interacts with an electromagnetic wave.

3.2.1. AFM phase - 100 polarization

In the low-energy region of 0-10 eV, peaks and fluctuations are observed in the dielectric function, indicating the presence of active electronic transitions within this energy range. Differences in these configurations can be easily observed, suggesting a potential responsiveness to modifications in the lower energy range. In the energetic range of 10-20 eV, we observe a gradual decrease in the dielectric function across various configurations, reaching a minimum of approximately 18-20 eV. This trend hints at a transition point where the real component of the dielectric constant decreases, reflecting a reduced level of polarization response. In the high-energy region (20-60 eV), as the configurations align after reaching the minimum, they gravitate towards a consistent value close to zero for ε_1. In fact, the material exhibits a subtle dielectric reaction. This behavior is quite common when the material moves into a zone where interband transitions are less prevalent.

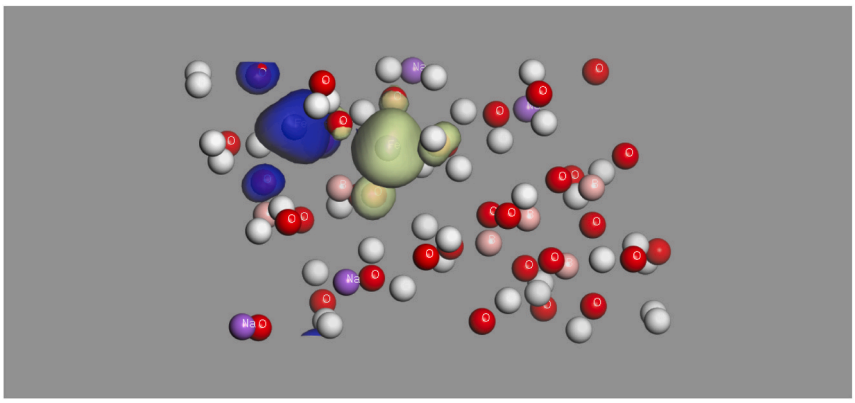

Fig. 8. The spin density of the AFM B1 configuration.

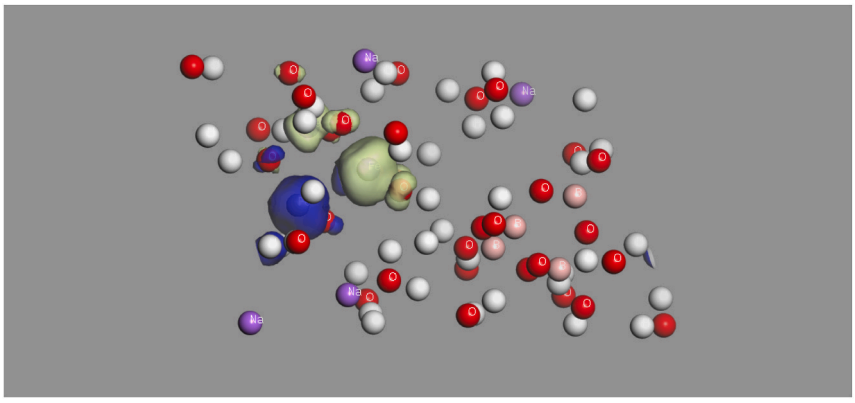

Fig. 9. The spin density of the AFM B1 configuration.

Table 3
Integrated spin densities of FM/AFM B1, B2, B1+B2.

	FM		AFM	
	Integrated Spin Density (ħ/2)	Integrated | Spin Density| (ħ/2)	Integrated Spin Density (ħ/2)	Integrated | Spin Density| (ħ/2)
B1	8.00000	8.17484	−0.130056E-12	9.16084
B2	8.00000	8.17344	−0.573259E-13	9.12497
B1+B2	16.0000	16.3051	−0.222531E-12	7.34018

The B1+B2 configuration typically exhibits a more substantial dielectric response when compared to other configurations in the lower energy spectrum, indicating a potential enhancement in polarization attributed to this specific structural arrangement. The B1 and B2 configurations exhibit comparable patterns, as shown in Fig. 14, yet they vary in magnitude, likely due to slight structural adjustments impacting the bonding atmosphere.

At specific energy ranges (0–25 eV), the imaginary part ε_2 displays noteworthy peaks, indicating interband electronic transitions, as illustrated in Fig. 15. The intensities of these peaks exhibit considerable variation across the different configurations. The peak of B2 (green curve) stands out the most at around 10 eV, showing a higher absorption in this range than B1+B2 (blue) and B1 (red). The B1+B2 combination (depicted by the blue curve) exhibits broader peaks with lower intensity, suggesting a wider variety of less pronounced transitions. The B1 (red curve) exhibits moderate peak intensities, demonstrating significant absorption within the 5 – 15 eV range. In the low-energy region of 0–5 eV, each of the three structures shows subtle yet noticeable absorption characteristics. These probably relate to transitions with low energy close to the Fermi level or shallow valence bands. The B1 structure appears to exhibit the most significant characteristics within this range, indicating enhanced light absorption at lower photon energies. In the middle energy range of 5 to 15 electron volts, you will find the predominant peaks representing all configurations. The prominent peak observed at approximately 10 eV for B2 indicates significant optical transitions, possibly stemming from electronic states with a high concentration at that energy level. In the high-energy region beyond 15 eV, the curves gradually decrease, showing minimal absorption. This suggests that fewer electronic transitions are occurring for higher photon energy, which demonstrates a reduction in the number of available electronic states within this range. The mixture of Fe-B interchanges in B1+B2 (blue) results in wider features with lower peak intensity than individual configurations, suggesting a more even distribution of optical transition energies. In configuration B1 (red), the peaks display a sharper, more defined appearance, implying stronger support for transitions at energy levels. B2 (green): The peak intensity is highest around 10 eV, indicating that the B2 configuration introduces additional active electronic states, thereby resulting in increased absorption. Absorption Strength: ε_2 peaks indicate intense light absorption at certain photon energies, with B2 showing the highest level of absorption within the 5–15 eV range. B2 is especially well-suited for applications that need high absorption in this energy range, like photothermal or photovoltaic devices. The wider absorption profile of B1+B2 indicates that this setup could be beneficial for a variety of applications, such as optoelectronics. The phenomenon of Electronic Structure Sensitivity highlights peaks in ε_2 that signify transitions between occupied and unoccupied electronic states. The distinctions among B1+B2, B1, and B2 highlight structural sensitivity, showcasing how atomic arrangements impact electronic state densities and transition probabilities. Magnetic phase and polarization go hand in hand: the AFM phase leads to a spin-induced division

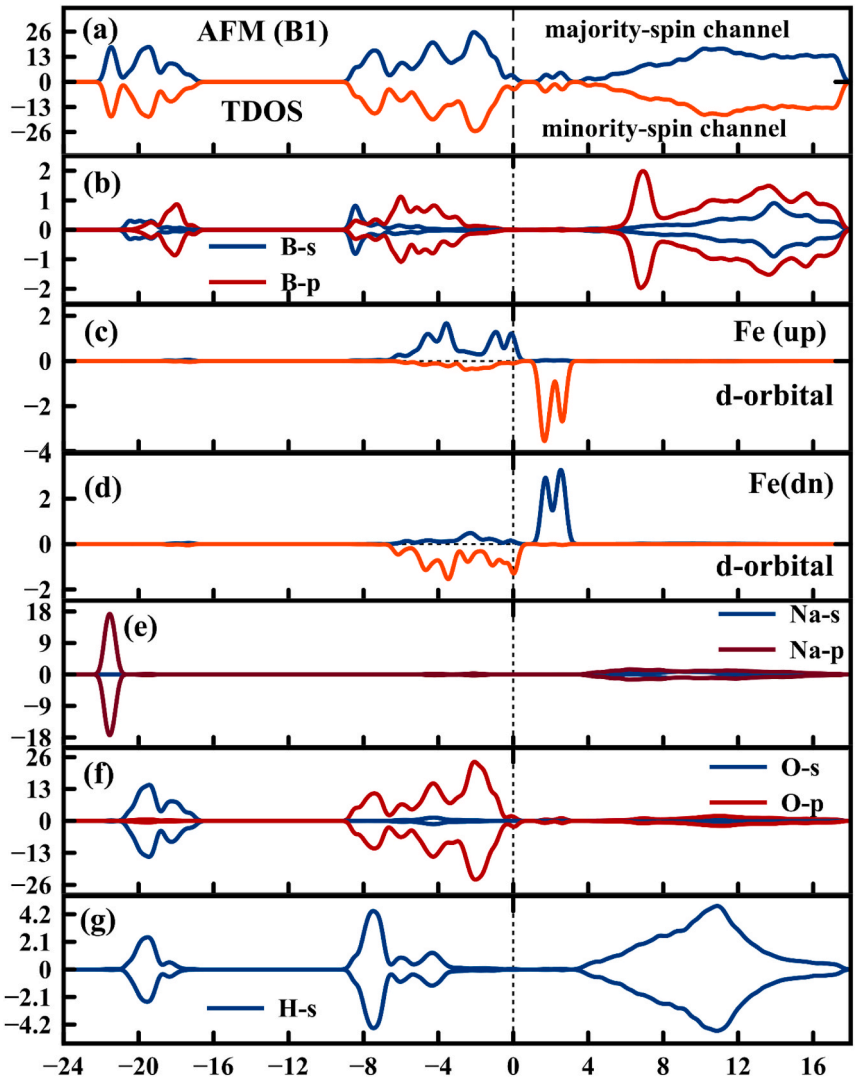

Fig. 10. **(a)** TDOS, PDOS of **(b)** B, **(c)** spin-up Fe, **(d)** spin-down Fe, **(e)** Na, **(f)** O, and **(g)** H of AFM B1.

in energy levels, potentially causing peaks in ε_2 to widen or move. The polarization of photons through 100 influences transition probabilities, potentially matching certain electronic orbitals.

3.2.2. *AFM phase - 010 polarization*

Fig. 16 portrays the real part (ε_1) of the dielectric function, which explains the material's dispersive characteristics. AFM ordering has an impact on the electronic band structure, consequently affecting the dielectric properties. The incident electromagnetic wave is oriented along the 010 direction, showing responsiveness to the material's anisotropy. In the low-energy region (0–10 eV), the dielectric function displays notable variation among different configurations, highlighting how sensitive the material's response at low energy is to Fe substitution.

The configuration of B1 exhibits the tallest peak in the area, indicating increased polarization effects or electron-cloud distortion due to Fe doping. A region with an energy range between 10 and 20 electron volts. Every configuration reveals a notable decrease in $\varepsilon 1$, resulting in negative values (suggestive of plasmonic characteristics or metallic-like reflection). Once surpassing 20 eV, the real part of the dielectric function exhibits convergence across all configurations. This indicates that transitions involving high energy are not significantly influenced by the substitution of Fe and are mainly governed by the inherent characteristics of the host tincal structure. Substituting Fe at various boron locations significantly alters the dielectric response within the low- and mid-energy ranges of 0 to 20 eV. This is probably a result of differences in electronic density and bonding specific to each site. AFM ordering affects the band structure, potentially leading to spin-polarized states that can affect optical transitions in the low-energy spectrum. The noticeable peaks and valleys observed in $\varepsilon 1$ imply that these materials could be customized for use in optoelectronics or plasmonics. For example, the presence of negative values within the 10–20 eV spectrum may suggest the material's potential for applications as a reflective or plasmonic substance within defined frequency bands.

The peaks in ε_2 indicate the energy intervals where notable optical absorption occurs, usually resulting from transitions between filled and unfilled electronic states. The magnetic phase known as AFM ordering exerts an influence on the DOS and transition probabilities, with a direct correlation to the absorption spectrum. In the low-energy region (0–10 eV), B1+B2 shows a slightly smaller peak than B1 and B2, hinting at a decrease in optical absorption when Fe substitutions are combined in this range. In this configuration, B2 showcases the most prominent characteristic, signifying heightened interband transitions, as shown in Fig. 17. This range reflects the shifts from shallow valence states to low-energy conduction bands. In the Intermediate Region, which ranges from 10 to 20 eV, all configurations exhibit prominent absorption peaks. Among them, configuration B1 demonstrates the highest peak at approximately 2.3, while B2 and B1+B2 follow closely behind. This peak is probably a result of transitions occurring between deeper

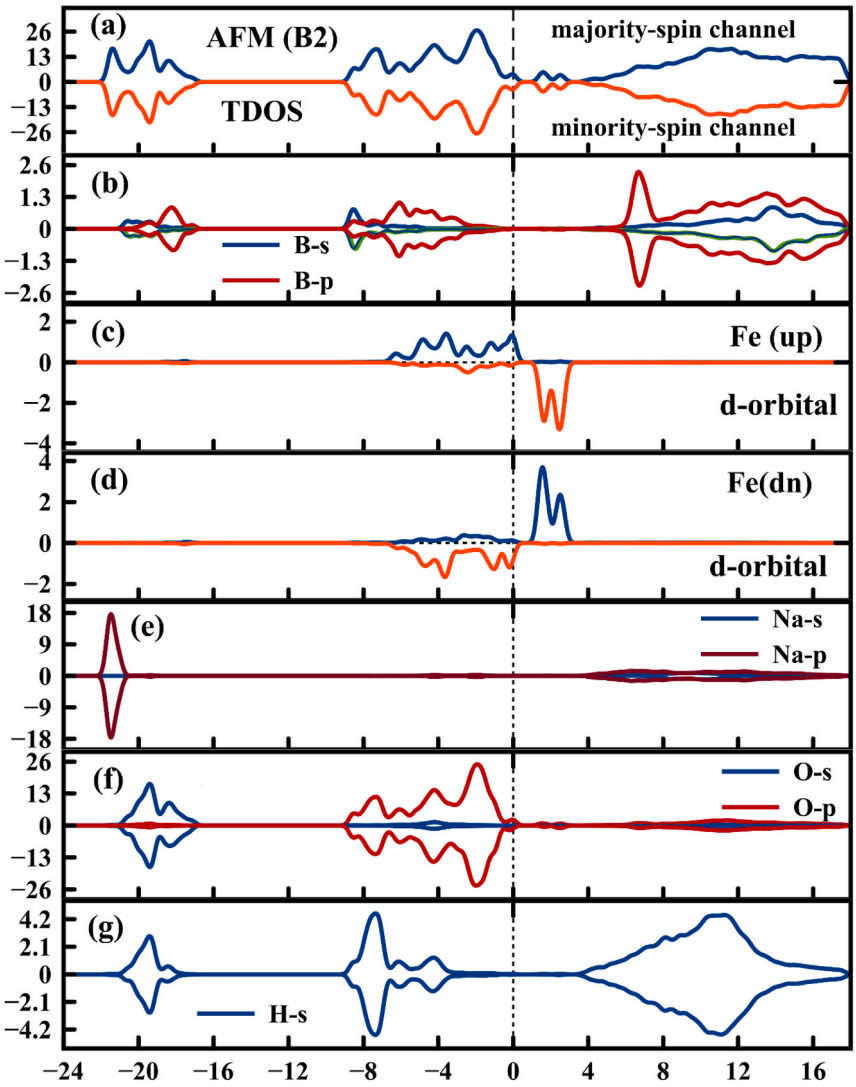

Fig. 11. **(a)** TDOS, PDOS of **(b)** B, **(c)** spin-up Fe, **(d)** spin-down Fe, **(e)** Na, **(f)** O, and **(g)** H of AFM B2.

valence states and higher-energy conduction bands. The variations in intensity emphasize how the substitution of Fe affects the electronic states that are accessible. In the high-energy region exceeding 20 eV, ε_2 starts to decrease quickly across all configurations, suggesting lower absorption levels at elevated photon energy. The coming together of curves in this range indicates that the high-energy electronic transitions are mainly influenced by the inherent traits of the host tincal structure, with Fe doping having a minor impact. Substituting Fe at various boron locations notably changes the absorption spectrum, especially within the 0–20 eV range. This can be explained by specific adjustments made to the electronic band structure of the site. The AFM ordering influences the DOS and spin selection rules, thus altering the intensity and location of peaks in ε_2.

3.2.3. *AFM phase - 001 polarization*

The parameter ε_1 starts with a high value for all configurations when photon energies are low, then steadily decreases, exhibiting noticeable fluctuations below approximately 20 eV before settling down to nearly consistent levels at energies above 20 eV. The low-energy behavior, below 20 eV, showcases the material's dispersive characteristics, whereas the stabilization at higher energy levels suggests a decrease in polarization response with increasing photon energy. In the low energy region (less than 10 eV), noticeable variations in both the intensity and form of $\varepsilon 1$ can be observed across the B1+B2, B1, and B2 configurations. B1, represented by the red curve, exhibits the most prominent peak within the 2–4 eV range, suggesting increased polarizability and refractive characteristics in this specific interval.

The green curve of B2 in Fig. 18 shows intermediate behavior, whereas the blue curve of B1+B2 displays lower values, indicating less polarization in comparison to B1. In the energy range of 10-20 eV, all curves gradually decrease towards zero, showing minor variations in their lowest points. The minima signify the photon energy at which electronic resonance effects or transitions hold sway. In the high-energy region exceeding 20 eV, the real part of the three configurations flattens and converges, suggesting that structural distinctions have a diminished effect on elevated photon energies. This behavior reflects the material nearing its asymptotic optical behavior, with a diminishing emphasis on electronic transitions. The photon's polarization along the 001 crystallographic direction hints that the disparities observed stem from the interaction of light waves with the material's anisotropic dielectric characteristics. This orientation has the power to enhance or hinder transitions depending on how electric fields align with bonding or orbital setups. Larger values of ε_1, like those seen in B1 within the 2–4 eV range, suggest elevated refractive indices, resulting in increased dispersion of the material in this setting. The reduction in ε_1 as photon energy increases indicates a decrease in dispersion, as the influence of electronic resonance effects lessens. The electronic polarizability is greatly influenced by structural arrangement, especially in the low-

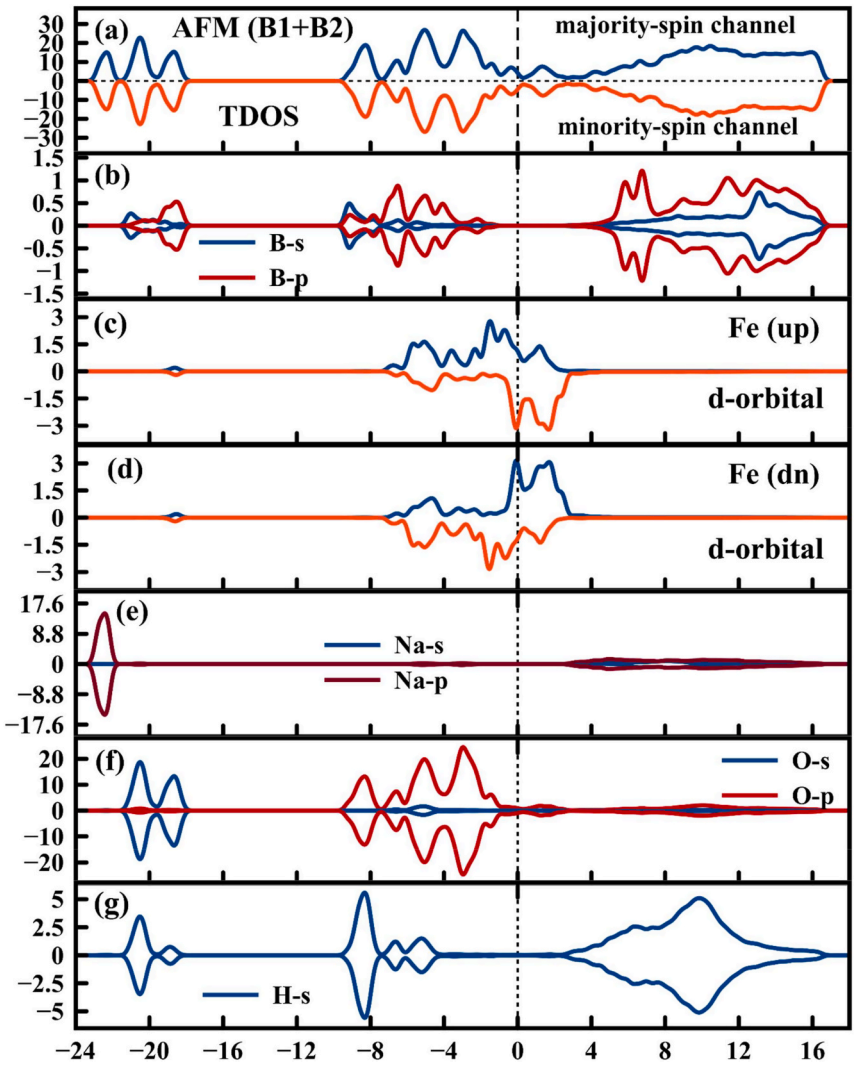

Fig. 12. **(a)** TDOS, PDOS of **(b)** B, **(c)** spin-up Fe, **(d)** spin-down Fe, **(e)** Na, **(f)** O, and **(g)** H of AFM B1+B2.

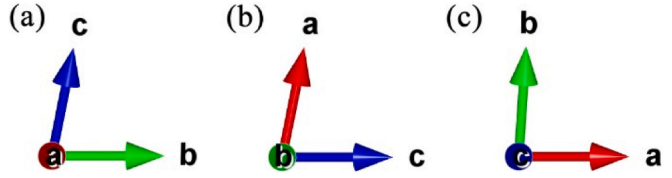

Fig. 13. The dielectric function and shielding efficiency are calculated separately for photons interacting with the tincal unit cell through certain directions.

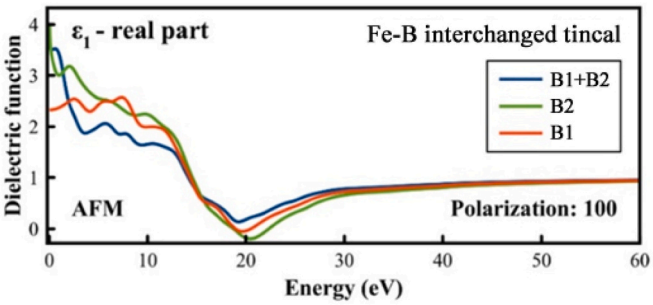

Fig. 14. The real part of the dielectric function calculated for 100 photon polarization of Tincal(B1), Tincal(B2), and Tincal(B1+B2) in the AFM phase.

energy range. B1, displaying the highest ε_1, implies increased dipole activity, potentially deriving from unique Fe-B bonding attributes or localized charge distributions. The significant variations observed between B1+B2, B1, and B2 underscore how dielectric properties are highly dependent on atomic configurations, demonstrating structural sensitivity. The combined B1+B2 arrangement presents a more consistent and subdued reaction, likely attributed to the smoothing impact of merging Fe-B exchanges.

All configurations show noticeable peaks below approximately 20 eV, suggesting active absorption within this energy range because of interband electronic transitions, as illustrated in Fig. 19. Once the photon energy surpasses 20 eV, the value of ε_2 tends towards zero, indicating low absorption at higher energy levels. In the low energy region (<10 eV), the red curve representing B1 stands out with a prominent peak, surpassing both B1+B2 (blue) and B2 (green) curves. This suggests that this configuration demonstrates the most potent electronic absorption within this range. The combination of B1 and B2 displays a slight reduction in absorption, possibly due to the combined impact of Fe-B exchanges. In the mid-energy region spanning from 10 to 20 eV, the green curve denoted as B3 exhibits a distinct peak between 13 and 15 eV, indicating heightened absorption due to electronic transitions specific to this structure. B1 exhibits a prominent secondary peak

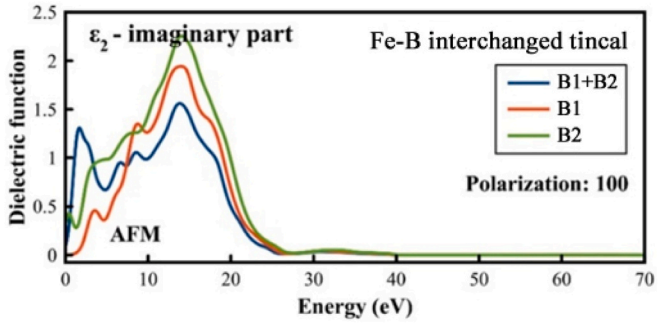

Fig. 15. The imaginary part of the dielectric function calculated in 100 photon polarization of Tincal(B1), Tincal(B2), and Tincal(B1+B2) in the AFM phase.

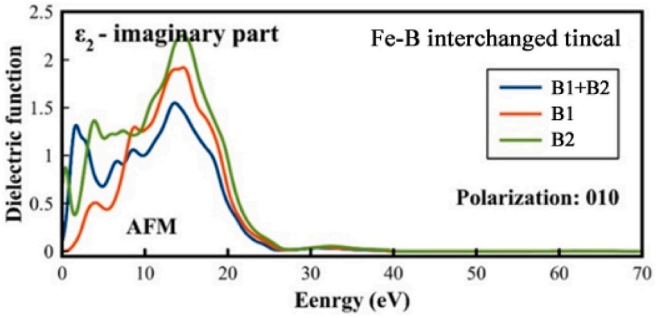

Fig. 17. The real part of the dielectric function calculated in the 010-photon polarization of Tincal(B1), Tincal(B2), and Tincal(B1+B2) in the AFM phase.

within this range, whereas B1+B2 consistently maintains lower levels, suggesting a reduced number of active states for photon absorption in this region. In the high-energy region (>20 eV), all configurations exhibit similar behavior, where $\varepsilon 2$ gradually decreases towards nearly zero, suggesting transparency and minimal absorption. The most significant absorption peak of B1 falls within the 7-10 eV range, indicating intense optical reactivity at this energy level because of electronic transitions that engage states located close to the Fermi level. B2 led its main peak slightly shifting towards higher energies (~13–15 eV), suggesting distinct electronic transition routes when compared to B1. The breadth of the peaks seen in B1 is greater when compared to B1+B2 and B2, suggesting a possible increase in the number of electronic states involved in the transitions. Absorption and Electronic Transitions: Variances in ε_2 across configurations emphasize how Fe-B atomic arrangements influence the electronic states and transitions that are accessible. The high absorption of B1 below 10 eV indicates that it possesses a more concentrated group of states near the valence and conduction bands, facilitating a greater number of transitions when exposed to photon stimulation. The peaks observed in ε_2 are indicative of photon energies that stimulate the movement of electrons from the valence band to the conduction band. The positions and intensities they exhibit mirror the distinct band structure traits found in each structural arrangement. Structural sensitivity is highlighted by a more discernible difference between B1+B2, B1, and B2 in ε_2 compared to ε_1, emphasizing the significance of Fe-B interchanges in influencing absorption properties. B1+B2 consistently exhibits the smallest ε_2, suggesting a decrease in optical absorption when compared to the remaining configurations. This characteristic might prove beneficial for applications that demand materials with minimal loss.

3.3. Shielding efficiency: comparing AFM and FM phases

Shielding efficiency (SE_T) values are negative across the entire

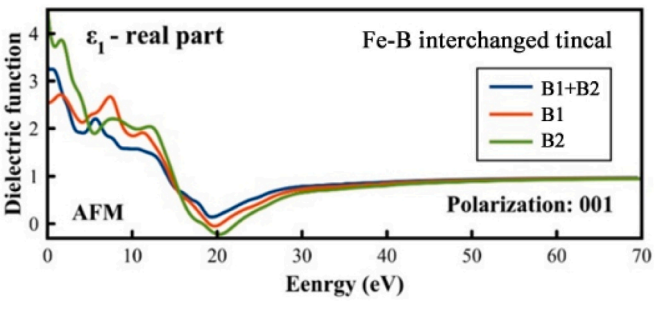

Fig. 18. The real part of the dielectric function was calculated in the 001-photon polarization of Tincal(B1), Tincal(B2), and Tincal(B1+B2) in the AFM phase.

energy range, indicating that the material absorbs rather than reflects electromagnetic energy when the polarization is along the 001 direction. This absorption characteristic proves to be advantageous for

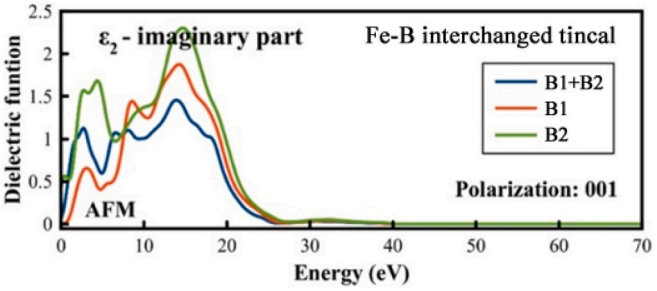

Fig. 19. The real part of the dielectric function was calculated in the 001-photon polarization of Tincal(B1), Tincal(B2), and Tincal(B1+B2) in the AFM phase.

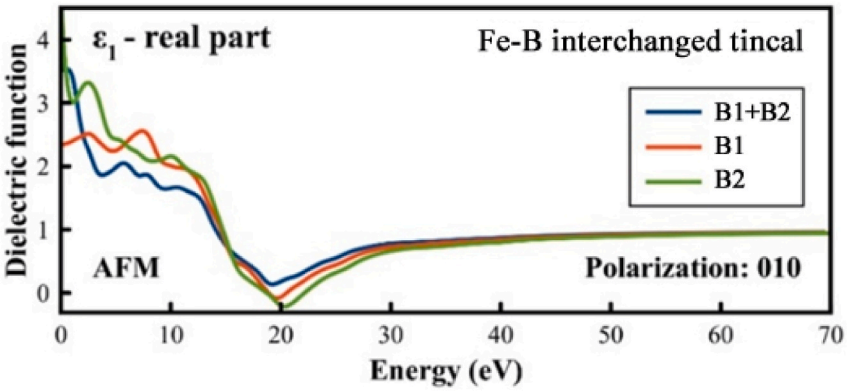

Fig. 16. The real part of the dielectric function was calculated in the 010-photon polarization of Tincal(B1), Tincal(B2), and Tincal(B1+B2) in the AFM phase.

applications that demand high-energy dissipation, like electromagnetic interference (EMI) shielding. At around 20 eV, both B1 (blue line) and B2 (red line) exhibit a notable dip in resonance. B2 displays a marginally more profound minimum compared to B1. This decline in the SE_T indicates an increase in absorption at this specific energy level, possibly resulting from electronic or magnetic resonance occurring within the material's structure. This could be linked to interactions within the material, affected by the AFM ordering.

Both B1 and B2 curves in Fig. 20 show oscillations, indicating the presence of several absorption resonances within the low-energy region (less than 30 eV). The oscillations observed could be a result of the interaction between electromagnetic waves and the internal structure of the material. These interactions are influenced by magnetic domain alignments and electronic transitions that are specific to the 001 polarization. Above 40 eV, the shielding efficiency of B1, B2, and the combined B1+B2 (black line) converges, indicating that at higher energies, the material's response becomes uniform and less affected by the specific polarization direction. This indicates that at high energies, the shielding behavior becomes more isotropic due to the dominance of the material's bulk properties. In essence, when polarized along the 001 direction, the material shows significant absorption characteristics with a prominent peak at approximately 20 eV, leading to maximal energy dissipation. The convergence observed at higher energies implies a reduction in directional dependency, whereas the distinct oscillations seen at lower energies underscore the intricate and anisotropic characteristics of the material's shielding response.

In Fig. 21, the oscillatory behavior below 20 eV is more noticeable for B2 (red line) than in the 001-polarization case. This indicates that the material's response may be influenced by the direction of polarization, possibly because of the anisotropy in its magnetic or electronic structure linked to its AFM arrangement. The dip around 20 eV in B2 is more pronounced in this plot, suggesting that the 010 polarization might have a stronger connection to certain absorption or resonance features in the material. Just like in the earlier plot, all three curves (B1, B2, and B1+B2) coincide above 40 eV. This convergence suggests that as photon energies increase, the significance of the polarization direction decreases, leading to the dominance of bulk properties in shielding behavior, rather than polarization-dependent resonances. The B1 curve (blue line) maintains its unique response compared to the B2 curve, though exhibiting slightly different oscillatory characteristics compared to the 001-polarization scenario. This variation further highlights that the electronic and magnetic structure of the material impacts its shielding behavior in different ways depending on the orientation of the incoming photons. The AFM with 010 polarization exhibits anisotropic shielding characteristics, displaying directional reliance on photon polarization at lower energies. It effectively absorbs energy over a wide spectrum, especially within the 10-30 eV range, with pronounced dips observed for both polarizations. This feature could come in handy for applications that need directional electromagnetic shielding, especially

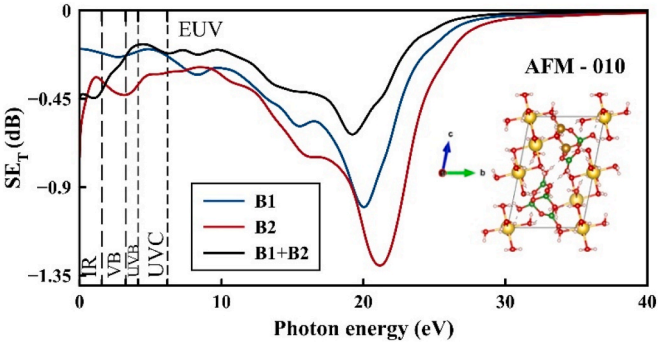

Fig. 21. Total shielding efficiency (SE_T) of AFM B1, B2, and B1+B2 as a function of photon energy that propagates through the b-axis.

when tailored for specific polarization orientations.

Note that in Fig. 22, negative shielding is commonly seen in materials that are efficient at dampening or absorbing incoming electromagnetic energy. The 001 polarization refers to the interaction of the photon with the host material through the c-axis. At energies below 20 eV, B1, B2, and B1+B2 exhibit unique responses. The B1 and B2 curves for the individual exhibit some oscillatory behavior, suggesting potential resonance or absorption features linked to the material's electronic or magnetic structure. At around 20 eV, both curves display a noticeable dip, with B1+B2 demonstrating the most pronounced minimum. This hints that, at this energy level, the material may exhibit increased absorption or a resonant interaction with incoming photons, which could be attributed to electronic transitions or collective excitations within the AFM structure. Above 40 eV, the three curves converge, showing that the shielding behavior becomes unaffected by the B1 and B2 configurations. This convergence may suggest that the material's reaction to electromagnetic radiation becomes less dependent on the specific magnetic or electronic setups and starts to demonstrate a more overarching characteristic of the material at these elevated photon energies. The B1 and B2 curves reveal distinct orientations or components in the magnetic and electronic structure, each contributing uniquely to the shielding behavior at lower energies. The discrepancies could stem from the AFM arrangement within the material. This arrangement of magnetic moments has the potential to impact the interaction between electromagnetic waves and the structure. The convergence at higher energies likely indicates the decreasing impact of magnetic ordering as photon energy rises, with electronic structure characteristics assuming greater importance. In an AFM material, the shielding behavior is anticipated to change depending on the magnetic ordering and the interaction of photons with the electronic states. Given that the incoming photons are directed along the a-b plane, the interaction is expected to highlight any variations in the electronic structure linked to the AFM alignment along the c-axis. The distinct dip at approximately

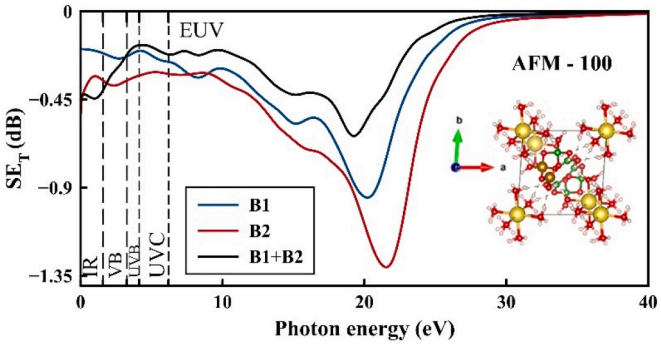

Fig. 20. Total shielding efficiency (SE_T) of AFM B1, B2, and B1+B2 as a function of photon energy that propagates through the a-axis.

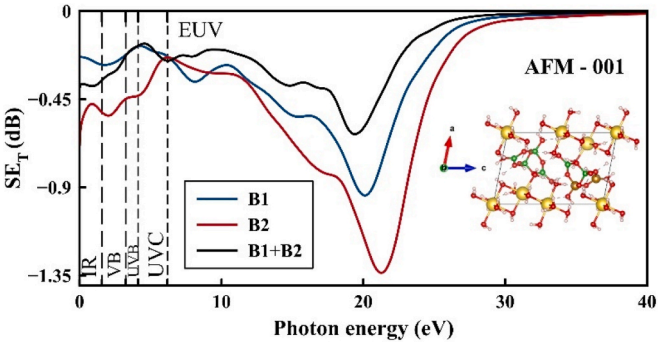

Fig. 22. Total shielding efficiency (SE_T) of AFM B1, B2, and B1+B2 structures as a function of photon energy that propagates through the c-axis.

20 eV, where all components play a crucial role in absorption, could be associated with interband transitions or magnon-related excitations that are unique to the material's AFM characteristics.

In both cases, B1 (blue line) and B2 (red line) show unique characteristics and oscillations, while the combined shielding efficiency (B1+B2, black line) illustrates the overall shielding performance of the material. Each curve exhibits distinct resonant characteristics at various energy levels, suggesting that B1 and B2 are responsive to different facets of the material's interaction with incident photons. The curves show variances between the 001 and 010 polarizations, especially in the energy ranges featuring distinct dips. For example, B2 in the 010 polarization exhibits a more pronounced oscillation below 20 eV than B2 in the 001 polarization. This implies that the material's response is influenced by directionality. This anisotropy likely stems from the AFM structure of the material, affecting its interaction with electromagnetic waves according to their polarization. The arrangement of magnetic orientations and crystal symmetries can lead to fluctuations in electronic and magnetic absorption. Both figures display significant decreases in shielding efficiency around 20 eV, with B1 and B2 reaching their lowest points. The dips may be linked to resonant absorption arising from electronic or magnetic excitations unique to this energy level. Above 40 eV energy levels, the curves for B1, B2, and B1+B2 come together in both figures, implying that the material's reaction becomes less influenced by polarization at higher photon energies. This coming together may suggest that the shielding at higher energies is primarily influenced by bulk characteristics, rather than resonances specific to orientation. The varying response to the 001 and 010 polarizations underscores how the material's anisotropic properties, specifically its AFM structure, influence its interaction with electromagnetic radiation. The B2 displays a stronger dip around 20 eV when aligned with 010 polarization. This observation could indicate a heightened resonance or absorption phenomenon in this orientation, potentially linked to distinct electronic transitions or sensitive magnon excitations aligned with the polarization direction.

Fig. 23 illustrates the overall shielding efficiency (SE_T) for the FM tincal structure with Fe and B atomic substitutions in configurations B1, B2, and B1+B2 when polarized through the 100 direction. In the low-energy range, the SE_T values remain negative, indicating that the material mainly absorbs electromagnetic energy rather than reflecting or blocking it. The B1 configuration (blue line) displays a series of oscillations, with the values dipping lower than B2 (red line). This suggests stronger energy dissipation at specific energy points for B1. The B1+B2 configuration (black line) typically presents as a blend of B1 and B2 responses, leading to more even oscillations. This indicates a collective shielding effect that harmonizes the absorption qualities of B1 and B2. Within this range, a significant decrease is observed around 20 eV. This phenomenon is most pronounced in the B1 configuration, with the SE_T reaching a minimum value below −0.7. This distinct dip observed in B1 could potentially be a result of resonance effects or energy dissipation associated with unique electronic or magnetic states originating from the Fe-B atomic substitution pattern. B2 also demonstrates a dip around this energy level, albeit not as pronounced, indicating distinct local structural or magnetic interactions that marginally lessen energy absorption. The B1+B2 configuration displays a similar dip, yet with a less noticeable minimum compared to when B1 is observed alone. This suggests that the combined substitutional pattern in this configuration results in a softened energy absorption characteristic. At elevated energy, all three arrangements gradually approach zero SE_T, indicating lessened interaction with the electromagnetic field at such energy levels. This convergence implies that at high photon energies, the material's absorbent properties decrease, rendering it more permeable to electromagnetic waves. Higher-energy photons tend to interact less with the atomic and magnetic structure. In comparison to the 001 and 010 polarization directions, the shielding trends in the 100 direction display consistent patterns overall. However, there are slight discrepancies in the SE_T values and oscillation intensities. The observed variations hint at the anisotropic shielding efficiency of the material, perhaps arising from structural or magnetic anisotropy in the alignment of Fe and B atoms. The way electromagnetic waves interact with a material is influenced by its particular orientation, which in turn affects the observed shielding behavior. As is the case with past polarizations, the consistently low SET values suggest that the material acts more as an absorptive medium and less as a reflective surface. The resonant and dissipative characteristics are connected to atomic-scale effects and potential magnetic interactions within the material. In short, the SE_T trends in the 100 polarizations show distinct absorption qualities, with a hint of directional responsiveness. The B1 configuration displays the highest energy dissipation around 20 eV. Meanwhile, B2 and B1+B2 demonstrate more gentle absorption. The behavior varies based on direction, showing disparities in SE intensity depending on polarization directions. This is probably caused by the anisotropic properties present in the FM tincal structure, which are influenced by Fe-B substitution patterns.

Fig. 24 illustrates the total shielding efficiency (SE_T) of the FM tincal structure with varying configurations of Fe and B atomic substitution. The configurations are labeled as B1, B2, and B1+B2, and the measurements were taken under polarization in the 010 direction. The shielding efficiency is graphed against energy (in eV), showing comparable overall trends as previously observed, albeit with slight variations attributed to the shift in polarization direction. In the low-energy region (0 to about 10 eV), all configurations exhibit negative SE_T values, signaling a preference for energy dissipation or absorption over reflection or blocking. The B1 configuration (blue line) displays the lowest SET value in this range, displaying a slightly deeper oscillation compared to B2 (red dotted line), hinting at stronger absorption or energy dissipation at energy levels. B1+B2 (black line) typically represents the average SE behaviors of B1 and B2, displaying smoother oscillations that may indicate a damping effect resulting from the combination of these configurations. In the intermediate energy range, the SE_T values decrease even more, reaching their lowest points at around 20 eV. This is

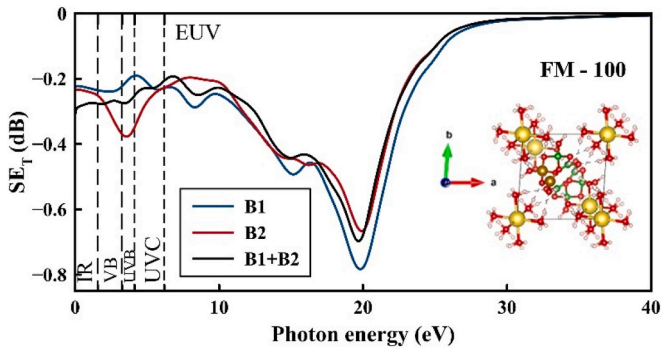

Fig. 23. Total shielding efficiency (SE_T) of FM B1, B2, and B1+B2 structures as a function of photon energy that propagates through the a-axis.

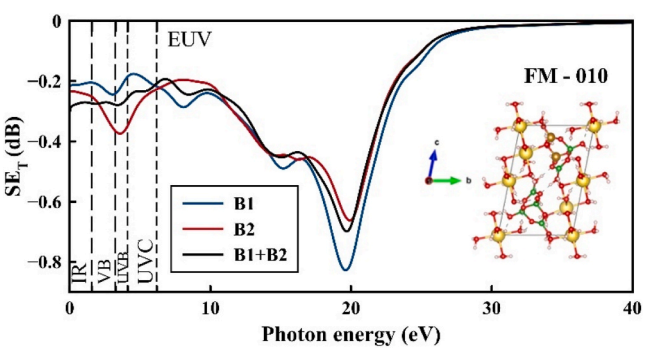

Fig. 24. Total shielding efficiency (SET) of FM B1, B2, and B1+B2 structures as a function of photon energy that propagates through the b-axis.

particularly notable for the B1 configuration, where SE_T dips below −0.8. This dip suggests a noteworthy absorption of energy or resonance effects at this energy level for the B1 configuration. This could be attributed to electronic states localized to the Fe-B substitution arrangement. The B2 configuration, despite exhibiting a slight decrease, does not drop as much as B1. This could be attributed to variances in how the atomic structure impacts electron density or magnetic response when exposed to the 010 polarization. B1+B2 follows a similar trend but has a slightly less intense drop, indicating that combining the two configurations results in a more balanced shielding behavior. Beyond 30 eV, the SE_T values for all three configurations (B1, B2, and B1+B2) converge toward zero, suggesting a decreased interaction with the incident electromagnetic energy. This indicates that as photon energies increase, the material starts to become more transparent to electromagnetic waves due to the decrease in absorption and dissipative effects. This behavior corresponds to the atomic-scale properties of the material, where photons of higher energy have reduced interaction with the structure. In comparison to the 001 polarized case, Fig. 19 shows parallel trends. However, the intensity and shape of the SE_T dips have been slightly altered. This implies that the shielding efficiency of this material is influenced by the polarization direction, possibly because of variations in the atomic and magnetic structure. The particular configuration of Fe and B atoms could impact the material's interaction with electromagnetic waves, varying according to distinct crystallographic orientations. The high dissipation is probably caused by resonance effects or interactions between electromagnetic waves and localized states introduced by the Fe-B substitution. The atomic-scale structure permits specific electronic transitions and magnetic responses that result in this absorptive behavior. In essence, this graph illustrates that the shielding efficiency in the 010 direction exhibits comparable qualitative characteristics with the 001 polarization. However, the specific SET values and dip intensities differ because of directional influences. The various Fe substitution configurations (B1, B2, and B1+B2) each present unique shielding features. B1 displays the most robust absorption around 20 eV, whereas B2 and B1+B2 show more moderate declines. The shielding behavior perceived in this scenario suggests a material response that is influenced by atomic substitution patterns and magnetic interactions.

Fig. 25 illustrates the overall shielding efficiency (SE_T) of FM tincal with three distinct atomic configurations: B1, B2, and B1+B2. In the specified setups, iron atoms have replaced boron atoms at different locations. The graph then illustrated the photon energy within the eV range, all under polarization in the 001 direction. At energies below 10 eV, all three configurations (B1, B2, and B1+B2) show relatively stable shielding efficiency. Both B1 and B2 exhibit minor oscillations individually. Between 10 and 30 eV, we noticed significant variations in the SET values between the different configurations. The B1 configuration (blue line) exhibits a significant dip, with values close to −0. 7 at around 20 eV, suggesting a robust absorption or lossy characteristic at this specific point. This might imply that this specific atomic arrangement vibrates more intensely at this energy level, resulting in increased energy dispersion. The B2 configuration (red line) also exhibits a dip in this energy range, albeit with slightly reduced intensity compared to B1. This suggests that the way Fe atoms are positioned in the B2 structure may influence their interaction with electromagnetic waves, perhaps as a result of alterations in atomic density or spatial configuration that impact resonance. The combination of B1+B2 configuration, represented by the black dashed line, appears to smooth out the spectral efficiency behavior of both B1 and B2, indicating a harmonious distribution of absorption properties among the combined atomic structures. When the energy surpasses 30 eV, all configurations (B1, B2, and B1+B2) converge towards an equilibrium value near zero. This suggests a decrease in the interaction with high-energy electromagnetic waves, which could mean that the material becomes more transparent to these waves. The convergence may suggest that at higher energies, the fine details of atomic substitution become less significant. The wavelength of incident energy becomes comparable to or smaller than interatomic distances, resulting in minimal shielding differences. Fe atoms might introduce localized magnetic and electronic states, resulting in unique resonance conditions based on their exact locations, and ultimately impacting the SE response. The configuration of B1+B2 could imply that incorporating Fe substitutions at various sites might help to balance out the SE response, resulting in a less pronounced dip when compared to B1 in isolation. The reliably negative SE values throughout the energy spectrum indicate that rather than obstructing electromagnetic waves, these materials could potentially absorb or facilitate partial transmission, particularly at the atomic level. This behavior aligns with materials that display resonant absorption rather than traditional reflection or scattering. Possibly, this effect is boosted by the atomic-scale interactions and the unique FM characteristics of the substituted Fe atoms. In essence, the various configurations (B1, B2, and B1+B2) of Fe-substituted tincal showcase unique electromagnetic shielding attributes, mainly influenced by their atomic alignment and resonant interactions. At intermediate energies, B1 exhibits the most pronounced absorption, whereas B2 and the combined configuration B1+B2 demonstrate comparatively lesser absorption. At elevated energy levels, the shielding effects decrease, suggesting minimal interaction with the electromagnetic waves within this range. The total shielding efficiency values of iron incorporated materials, production methods, and frequency of EM are given in Table 4.

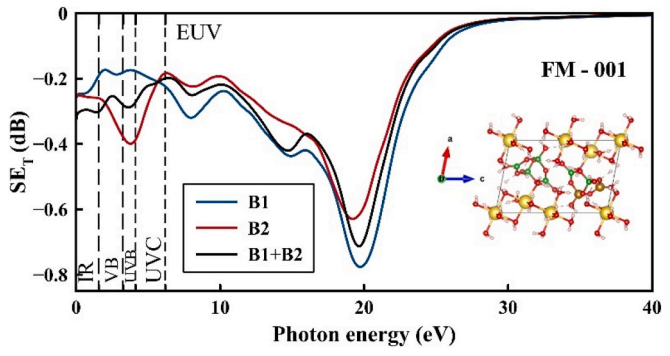

Fig. 25. Total shielding efficiency (SE_T) of FM B1, B2, and B1+B2 structures as a function of photon energy that propagates through the c-axis.

The analysis of microwave absorbers and EMI shielding materials reveals diverse performance capabilities across Fe-based composites, showcasing their suitability for various technological applications. Among the studied materials, Fe_xNi_{1-x}@PVDF@MWCNT stands out with the highest SE value of −58 dB within the 8–12 GHz frequency range, indicating its potential for efficient and compact EMI shielding. Similarly, $Mn_xFe_{3-x}O_4$ spherical chains and $Ba_{2-x}Dy_xZn_2Fe_{28-y}Mn_yO_{46}$ exhibit high SE values of −52.8 dB at 10 GHz and −55 dB at 11.62 GHz, respectively. These materials highlight the effectiveness of Fe-based absorbers in achieving strong shielding with relatively low material usage, making them ideal for lightweight applications. Coin-like Fe [24] demonstrates an impressive SE of −53.2 dB at 16 GHz, emphasizing the role of unique morphologies in enhancing performance. Additionally, $BaFe_{12-x}Ti_xO_{19}$ composites achieve −30.7 dB at 5.67 GHz, indicating their potential for low-frequency shielding. The sol-gel and solvothermal synthesis methods employed for these materials further showcase the versatility of chemical processing techniques in tailoring absorber properties. Iron nanowires (NWs) dispersed in epoxy resin achieved SE values of 32 dB at 1.1 GHz, while NWs in paraffin wax exhibit 29.7 dB at 5 GHz. Carbonyl iron fibers in polyurethane foam also deliver 25 dB SE at 10 GHz, providing an alternative approach for lightweight structural integration. $Ni_{0.8}Zn_{0.2}Ce_{0.06}Fe_{1.94}O_4$/GNS reaches −37.4 dB at 12.3 GHz, indicating the effectiveness of combining Fe components with carbonaceous materials for strong absorption in the microwave frequency range. Meanwhile, $Sr_{0.8}La_{0.2}Fe_{11.8}Co_{0.2}O_{19}$-60%Fe achieves −30 dB at 8 GHz, suggesting that incorporating multiple Fe components

Table 4
Fe-based microwave absorber.

Material	Method	SE_T (dB)	f (GHz)	Ref.
Porous Fe particles	Corrosion technique	−42.2	13.2	[20]
Hexagonal Fe flakes	Hydrothermal	−15.3	12.2–16.6	[21]
Fe nanoparticles	Ball milling	−23.67	15.24	[22]
Fe dendritic	Hydrothermal	−25	2.5	[23]
Coin-like Fe	Reduction	−53.2	16	[24]
$Mn_xFe3_{-x}O_4$ spherical chains ($x = 0.74$)	Solvothermal	−52.8	10	[25]
$Co_xFe_{3-x}O_4$ ($x = 0.9$)	Solvothermal	−41.09	12.08	[26]
$Sr_{1-x}Nd_xFe_{12-x}Co_xO_{19}$ ($x = 0.4$)	Sol–gel, autocombustion	−22	16.2	[27]
$BaFe_{12-x}Ti_xO_{19}$/CI ($x = 0.2$)	Sol-gel, physical blending	−30.7	5.67	[28]
$Ba_{2-x}Dy_xZn_2Fe_{28-y}Mn_yO_{46}$	Sol–gel	−55	11.62	[29]
$BaSrCo_{2-x}Ni_xFe_{12}O_{22}$ ($x = 0.5$)	Solid-state reaction	>−45	12	[30]
$BaSr_{0.5}CoZnFe_{12-x}Al_xO_{22}$ ($x = 0.3$)	Sol-gel	−19	11.5	[31]
$Sr(MnTi)_xCoZnFe_{12-2x}O_{19}$ ($x = 1$)	Aqueous combustion	−22.7	11.5	[32]
$Ba_{0.5}Sr_{0.5}Co_xW_xFe_{12-x}O_{19}$ ($x = 0.2$)	Ceramic	−15.2	11.22	[33]
Fe_xNi_{1-x}@PVDF@MWCNT	Acid treatment, melt mixing	−58	8–12	[34]
$Sr_{0.8}La_{0.2}Fe_{11.8}Co_{0.2}O_{19}$-60%Fe	Chemical vapor deposition	−30	8	[35]
$Ni_{0.8}Zn_{0.2}Ce_{0.06}Fe_{1.94}O_4$/GNS	Sol-gel deoxidation technique	−37.4	12.3	[36]
Carbonyl iron fibers	Polyurethane foam	25	10	[37]
Iron NWs	Epoxy resin	32	1.1	[38]
Iron NWs	Paraffin wax	29.7	5	[39]
LIG - La3Fe5O12	solid-state reaction	[2.2, 3.2]	12-18	[40]
$Ni_{80}Fe_{20}$ (NF)/cement	mixing	22.17	12.4	[41]
Iron oxide/CNT-based artificial nacre	mineralization	~29.74	18	[42]
iron-decorated polypyrrole-fly ash composite (Fe-ppy-25%FA)	chemical oxidative polymerization	~19	S-band	[43]
Fe-doped Tincal	GGA/PBESol	FM: [-0.6,-0.8] AFM: [-0.6,-1.4]	EUV	**This work**

can provide balanced performance across SE, frequency range. Besides, SE_T values vary between 3.1 dB and ~2.2 dB with a slightly decreasing behavior from 12 to 18 GHz frequency of EM for 10 wt% Lanthanum Iron Garnet (LIG) ($La_3Fe_5O_{12}$) into the epoxy matrix [40]. Yan et al. focus on iron ore tailings/cement composite, resulting in a 22.17 dB shielding efficiency under 12.4 GHz frequency for the filling of 5 wt% iron oxide (Fe_3O_4) nanoparticles into the cement composite [41]. UV-blue light-shielding rate of FT-PU nanocomposite films is found to be 99.93% in UVB (280-320 nm), 93.91% in UVA (320–400 nm), 50.73% in blue (400–500 nm), and 80.93% in Ave-T (500–800 nm) [42]. NIR and MIR reflectance of poly (Vinylidene Fluoride-co-Hexafluoropropylene) films filled with iron nanoparticles are revealed by Ref. [43]. The typical decrease in IR transmittance for 1, 2.5, 5, 10, and 50 mg of iron NPs is approximately 13%, 24%, 31%, 77%, and 98%, respectively. IR shielding characteristics of the PolyVinylidene Fluoride-co-Hexafluoropropylene (PVDF-HFP) films can be efficiently adjusted by incorporating the correct quantity of the Fe nanoparticles [44]. Moreover, an artificial nacre, which is formed by CNT and iron, demonstrates remarkable shielding effectiveness (SE_T: 17–30 dB, peaking at 29.74 dB at 18 GHz). Its shielding primarily relies on absorption, which dominates above 9 GHz, and the nacre-inspired structure ensures robustness, retaining 70–96% performance [45]. Basavaraia et al. revealed that Fe-Ppy-25%FA, which is an iron-decorated polypyrrole fly ash nanocomposite, shows an EMI shielding effectiveness of ~19 dB in the S-band [46]. Besides, Lanthanum oxide incorporated lead borate, Nd2O3 doped TeO2–ZnO, and Ge–Sb–S chalcogenide glasses show the impact of the dopant, and variety in guest on shielding literature [47–49]. High SE values often correlate with specific frequencies and thicknesses, with lightweight and low-thickness materials achieving notable success in targeted applications. The integration of Fe-based components, alloying, and carbonaceous structures demonstrates immense versatility, while the use of sol-gel, solvothermal, and other innovative synthesis techniques continues to expand the functionality and applicability of these materials. This work introduces a novel structure, even though the shielding efficiency values are not notable when compared to the above-mentioned iron-incorporated systems.

In the extreme ultraviolet (EUV) band, shielding is primarily applied in a few highly specialized fields, as EUV radiation is strongly absorbed by almost all materials, making shielding more about containment, reflection control, or selective filtering rather than traditional blocking. The main application areas are EUV Lithography (semiconductor manufacturing), space science and solar physics, EUV/soft X-ray optics and synchrotron facilities, and plasma physics and fusion research. Shielding is essential in EUV lithography machines. The objectives are to keep the EUV radiation produced by the plasma source inside the vacuum chamber, shield operators and machine parts from scattered or leaked EUV rays that could contaminate or damage them, and use multilayer mirror coatings as shields by selectively reflecting EUV while absorbing other wavelengths. Since EUV is photon radiation rather than electromagnetic interference in the radio/microwave sense, no traditional EMI-like shielding is applicable. In conclusion, EUV shielding—-which focuses on vacuum conditions, spectral filtering, and controlled reflection—is a specialized and crucial application in semiconductor manufacturing, space telescopes, sophisticated optics, and plasma research [50–52].

4. Conclusion

For many years, there has been interest in the idea of shielding to reduce undesired radiation across a wide spectrum, particularly in relation to security and health. The theoretical calculation of the shielding efficiency (SE) of Fe-doped tincal nanoparticles using DFT and a proven methodology is the main subject of this study. The GGA with the Koelling-Harmon relativistic correction and the PBEsol functional was used in the computations. Both the FM and AFM states of the dopant were taken into account when treating the Fe-doped tincal structures. The most advantageous condition was determined to be AFM. Furthermore, unlike raw tincal, which has a broad bandgap, the doped structure shows conductive conductivity.

For incoming photons, the materials under investigation have almost the same shielding efficiency (SE) along the [010] and [100] projections. However, they vary along the [001] projection. This suggests that the in-plane and out-of-plane shielding efficiency exhibit optical anisotropy, a property that is similarly impacted by the dopant configurational variations.

Comparing the FM and AFM states, the SE of the AFM state is wider throughout the spectrum than that of the FM state. For photon energies between 15 and 20 eV, the highest SE is noted. For all configurations taken into consideration, the Fe-B interchanged tincal structures show comparatively low shielding efficiency. Moreover, these materials' major shielding properties are limited to the extreme ultraviolet (EUV) spectrum. Total shielding efficiency is between −0.6 and −0.8 for the FM phase, while the AFM phase provides higher values, which are between −0.6 and −1.4.

Data statement

The data for this study was obtained from the CASTEP codes.

Prime novelty statement

Please find enclosed our paper entitled "Shielding efficiency of iron doped tincal: A first-principles study" which we hope will be suitable for publication in Physica B: Condensed Matter.

This work aims to enlighten the shielding efficiency of iron incorporated tincal. According to our best knowledge, this content is being conducted for the first time. The proposed method simply based on ab-initio calculations. Density functional theory in GGA-PBESol scheme is preferred. The incorporation means interchanging of iron with distinct boron sites. Hence, Fe-B and Fe-O bonds appear in the structure. The photon energy is exposed to considered structure through various projections. The shielding efficiency (SE) is calculated for all. In each case, SE is obtained from the dielectric function which is calculated by Kramer's Kronig relations. The authors performed all runs and keep following a traditional pipeline using CASTEP package.

The primary results are as follows. Ultraviolet (UV), Infrared (IR) and Visible Region (VR) SE are revealed. Even the results point out a poor/weak shielding, the content of paper provide a powerful flow to describe the shielding efficiency of a crystal. Besides, antiferromagnetic state is favored instead of ferromagnetism by guest atom (iron) on behalf of whole unit cell. The best shielding performance is for extreme UV region. Additionally, the increasing number of iron is not decisive in dielectric response.

This study has not already been published or submitted for publication elsewhere. The authors declare to have no conflict of interest regarding this study and have contributed significantly to the work and are in agreement with the content of the manuscript.

CRediT authorship contribution statement

I.P. Duru: Conceptualization, Data curation, Formal analysis, Investigation, Methodology, Software, Validation, Visualization, Writing – original draft, Writing – review & editing. **E. Ozugurlu:** Funding acquisition, Project administration, Writing – review & editing. **L. Arda:** Supervision.

Declaration of competing interest

The authors declare that they have no known competing financial interests or personal relationships that could have appeared to influence the work reported in this paper.

Acknowledgements

This work was supported by the Research Fund of Istanbul Technical University (TGA-2021-42846). Computing resources used in this work were provided by the National Center for High-Performance Computing of Istanbul Technical University (UHEM), Türkiye under grant number 1006342019.

Data availability

Data will be made available on request.

References

[1] S. Geetha, K.K. Satheesh Kumar, C.R.K. Rao, M. Vijayan, D.C. Trivedi, EMI shielding: methods and materials—A review, J. Appl. Polym. Sci. 112 (4) (2009) 2073–2086, https://doi.org/10.1002/app.29812.

[2] E. Zornoza, G. Catalá, F. Jiménez, L. García Andión, P. Garcés, Función de apantallamiento de interferencia electromagnética de pastas de cemento con materiales carbonosos y cenizas volantes procesadas, Mater. Construcción 60 (300) (2010) 21–32, https://doi.org/10.3989/mc.2010.51009.

[3] S. Ghosh, D. Mondal, R. Ganguly, S. Das, N.C. Das, Fabrication of reduced graphene oxide/silver nanoparticles decorated conductive cotton fabric for high-performing electromagnetic interference shielding and antibacterial application, Fibers Polym. 20 (6) (2019) 1161–1171, https://doi.org/10.1007/s12221-019-1001-7.

[4] H. Üşenti, I.P. Duru, Investigation of the electromagnetic shielding efficiency of FeB and Fe2B: ab-initio calculations, Model. Simulat. Mater. Sci. Eng. 32 (8) (2024) 085007, https://doi.org/10.1088/1361-651X/ad836a.

[5] A.K. Singh, A. Shishkin, T. Koppel, N. Gupta, A review of porous lightweight composite materials for electromagnetic interference shielding, Composites, Part B Eng. 149 (2018) 188–197, https://doi.org/10.1016/j.compositesb.2018.05.027.

[6] I. Araz, The measurement of shielding effectiveness for small-sized ferrite-based flat materials, Turk, J. Electr. Eng. Comput. Sci. 26 (6) (2018) 2996–3006, https://doi.org/10.3906/elk-1803-162.

[7] S. Sankaran, K. Deshmukh, M.B. Ahamed, S.K.K. Pasha, Electrical and electromagnetic interference (EMI) shielding properties of hexagonal boron nitride nanoparticles reinforced polyvinylidene fluoride nanocomposite films, Polym.-Plast. Technol. Eng. 58 (11) (2018) 1191–1209, https://doi.org/10.1080/03602559.2018.1542725.

[8] M. Ou, H. Liu, H. Qin, N. Hu, S. Wang, Z. Liu, H. Li, Y. Zhang, Ultra-flexible and high-performance electromagnetic wave shielding film based on CNTF/Liquid metal composite films, J. Appl. Phys. 125 (13) (2019) 134906, https://doi.org/10.1063/1.5089579.

[9] V. Shukla, Review of electromagnetic interference shielding materials fabricated by iron ingredients, Nanoscale Adv. 1 (5) (2019) 1640–1671, https://doi.org/10.1039/c9na00108e.

[10] X.T.A. Chu, V.D. Dao, H.-I. Kim, D.K. Choi, H.-S. Kim, Microwave absorption properties of iron nanoparticles prepared by ball-milling, J. Electron. Mater. 45 (5) (2016) 2311–2315, https://doi.org/10.1007/s11664-015-4248-9.

[11] R.C. Che, C.Y. Zhi, C.X. Liang, X.G. Zhou, Microwave absorption enhancement and complex permittivity and permeability of Fe encapsulated within carbon nanotubes, Adv. Mater. 16 (5) (2004) 401–405, https://doi.org/10.1002/adma.200306460.

[12] M. Chirita, I. Grozescu, Fe2O3–nanoparticles, physical properties and their photochemical and photoelectrochemical applications, Chem. Bull. 54 (68) (2009) 1–8. https://dspace.upt.ro/xmlui/handle/123456789/1041.

[13] K. Momma, F. Izumi, VESTA 3 for three-dimensional visualization of crystal, volumetric, and morphology data, J. Appl. Crystallogr. 44 (6) (2011) 1272–1276, https://doi.org/10.1107/s0021889811038970.

[14] J.P. Perdew, A. Ruzsinszky, G.I. Csonka, O.A. Vydrov, G.E. Scuseria, L. A. Constantin, X. Zhou, K. Burke, Restoring the density-gradient expansion for exchange in solids and surfaces, Phys. Rev. Lett. 100 (13) (2008) 136406, https://doi.org/10.1103/physrevlett.100.136406.

[15] M.D. Segall, P.J.D. Lindan, M.J. Probert, C.J. Pickard, P.J. Hasnip, S.J. Clark, M. C. Payne, First-principles simulation: ideas, illustrations and the CASTEP code, J. Phys. Condens. Matter 14 (11) (2002) 2717–2744, https://doi.org/10.1088/0953-8984/14/11/301.

[16] C. Li, Q. Hou, Effects of Y doping with point defects on the ferromagnetic properties of ZnO (0001)-Zn polar surface, Appl. Surf. Sci. 459 (2018) 393–396, https://doi.org/10.1016/j.apsusc.2018.08.018.

[17] Q. Hou, X. Jia, Z. Xu, C. Zhao, L. Qu, Effects of Li doping and point defect on the magnetism of ZnO, Ceram. Int. 44 (2) (2018) 1376–1383, https://doi.org/10.1016/j.ceramint.2017.09.162.

[18] X. Jia, Q. Hou, Z. Xu, L. Qu, Effect of Ce doping on the magnetic and optical properties of ZnO by the first principle, J. Magn. Magn Mater. 465 (2018) 128–135, https://doi.org/10.1016/j.jmmm.2018.05.088.

[19] R. Singh, H.L. Huang, C.H. Lai, et al., Symmetry driven altermagnetic spin splitting in hexagonal CrTe from first principles, Sci. Rep. 16 (2026) 10458, https://doi.org/10.1038/s41598-026-38641-1.

[20] G. Tong, W. Wu, Q. Hu, J. Yuan, R. Qiao, H. Qian, Enhanced electromagnetic characteristics of porous iron particles made by a facile corrosion technique, Mater. Chem. Phys. 132 (2–3) (2012) 563–569, https://doi.org/10.1016/j.matchemphys.2011.11.070.

[21] L.S. Fu, J.T. Jiang, C.Y. Xu, L. Zhen, Synthesis of hexagonal Fe microflakes with excellent microwave absorption performance, CrystEngComm 14 (20) (2012) 6827–6832, https://doi.org/10.1039/c2ce25836f.

[22] C.M. Shang, G.J. Ji, W. Liu, X.M. Zhang, H.L. Lv, Y.W. Du, One–pot in situ molten salt synthesis of octahedral Fe3O4 for efficient microwave absorption application, RSC Adv. 5 (100) (2015) 80450–80456, https://doi.org/10.1039/c5ra15949k.

[23] G. Sun, B. Dong, M. Cao, B. Wei, C. Hu, Hierarchical dendrite-like magnetic materials of Fe3O4, γ-Fe2O3, and Fe with high performance of microwave absorption, Chem. Mater. 23 (6) (2011) 1587–1593. https://pubs.acs.org/doi/pdf/10.1021/cm103441u.

[24] H. Lv, X. Liang, G. Ji, H. Zhang, Y. Du, Porous three–dimensional flower-like Co/CoO and its excellent electromagnetic absorption properties, ACS Appl. Mater. Interfaces 7 (18) (2015) 9776–9783, https://doi.org/10.1021/acsami.5b01654.

[25] Y. Li, T. Wu, K. Jiang, G. Tong, K. Jin, N. Qian, L. Zhao, T. Lv, Mn2+ induced structure evolution and dual-frequency microwave absorption of MnxFe3−xO4 hollow/porous spherical chains made by a one-pot solvothermal approach, J. Mater. Chem. C 4 (29) (2016) 7119–7129, https://doi.org/10.1039/C6TC01900E.

[26] R. Ji, C. Cao, Z. Chen, H. Zhai, J. Bai, Solvothermal synthesis of CoxFe3–xO4 spheres and their microwave absorption properties, J. Mater. Chem. C 2 (29) (2014) 5944–5953, https://doi.org/10.1039/c4tc00167b.

[27] Z. Zhang, X. Liu, X. Wang, Y. Wu, R. Li, Effect of Nd–Co substitution on magnetic and microwave absorption properties of SrFe12O19 hexaferrites, J. Alloys Compd. 525 (2012) 114–119, https://doi.org/10.1016/j.jallcom.2012.02.088.
[28] W. Feng, Y. Cao, J. Gang, W. Su, Preparation and microwave absorption property of BaFe12-xTixO19/carbonyl iron powder nanocomposites, Integrated Ferroelectrics Int. J. 189 (1) (2018) 63–70, https://doi.org/10.1080/10584587.2018.1456159.
[29] I. Sadiq, S. Naseem, S. Riaz, S.S. Hussain, H.M. Khan, M.N. Ashiq, M. Rana, Study of structural, magnetic and microwave absorption properties of Dy-Mn substituted nanosized material in X-band frequency range, J. Alloys Compd. 715 (2017) 284–290, https://doi.org/10.1016/j.jallcom.2017.03.033.
[30] C.A. Stergiou, G. Litsardakis, Y-type hexagonal ferrites for microwave absorber and antenna applications, J. Magn. Magn Mater. 405 (2016) 54–61, https://doi.org/10.1016/j.jmmm.2015.12.027.
[31] Y. Song, J. Zheng, M. Sun, M. Wang, L. Ji, Z. Xu, H. Sun, Y. Liu, The electromagnetic and microwave absorbing properties of polycrystalline Y-type Ba1.5Sr0.5CoZnFe12−xAlxO22 hexaferrites over the microwave range, J. Mater. Sci. Mater. Electron. 27 (4) (2016) 4131–4138, https://doi.org/10.1007/s10854-016-4272-4.
[32] C. Yuan, Y. Tuo, Microwave adsorption of Sr(MnTi)xFe12−2xO19 particles, J. Magn. Magn Mater. 342 (2013) 47–53, https://doi.org/10.1016/j.jmmm.2013.04.038.
[33] R. Joshi, C. Singh, D. Kaur, S.B. Narang, R. Jotania, Microwave absorption characteristics of Co2+ and W4+ substituted M-type Ba0.5Sr0.5CoxWxFe12−2xO19 hexagonal ferrites, J. Mater. Sci. Mater. Electron. 28 (1) (2017) 228–235, https://doi.org/10.1007/s10854-016-5515-0.
[34] V. Bhingardive, S. Suwas, S. Bose, New physical insights into the electromagnetic shielding efficiency in PVDF nanocomposites containing multiwall carbon nanotubes and magnetic nanoparticles, RSC Adv. 5 (101) (2015) 79463–79472, https://doi.org/10.1039/C5RA13901E.
[35] Z. Zhang, X. Liu, X. Wang, Y. Wu, Y. Liu, Electromagnetic and microwave absorption properties of Fe–Sr0.8La0.2Fe11.8Co0.2O19 shell-core composites, J. Magn. Magn Mater. 324 (13) (2012) 2177–2182, https://doi.org/10.1016/j.jmmm.2012.02.107.
[36] X. Yuan, L. Leng, H. Huang, X. Chen, H. Wang, Z. Xiao, Y. Zhai, H. Chen, G. Zeng, Speciation and environmental risk assessment of heavy metal in bio-oil from liquefaction/pyrolysis of sewage sludge, Chemosphere 120 (2015) 645–652, https://doi.org/10.1016/j.chemosphere.2014.10.010.
[37] M. Yu, X. Li, R. Gong, Y. He, H. He, P. Lu, Magnetic properties of carbonyl iron fibers and their microwave absorbing characterization as the filler in polymer foams, J. Alloys Compd. 456 (1–2) (2008) 452–455, https://doi.org/10.1016/j.jallcom.2007.02.106.
[38] X. Li, X. Guo, T. Liu, X. Zheng, J. Bai, Shape-controlled synthesis of Fe nanostructures and their enhanced microwave absorption properties at L-band, Mater. Res. Bull. 59 (2014) 137–141, https://doi.org/10.1016/j.materresbull.2014.07.016.
[39] P.-A. Yang, H. Ruan, Y. Sun, R. Li, Y. Lu, C. Xiang, Excellent microwave absorption performances of high length-diameter ratio iron nanowires with low filling ratio, Nanotechnology 31 (39) (2020) 395708, https://doi.org/10.1016/j.materresbull.2014.07.016.
[40] N.I.Z. Azman, M.A.A. Zaini, N.A.M.N. Hamid, R. Nazlan, M.A. Jusoh, Electromagnetic shielding effectiveness of epoxy/lanthanum iron garnet (LIG) nanocomposites at Ku-band frequency, Mater. Today Proc. 51 (2) (2022) 1432–1436, https://doi.org/10.1016/j.matpr.2021.12.084.
[41] Y. Yan, X. Du, Y. Kuang, Study on the influence of nickel-iron alloy powder on the mechanical strength and electromagnetic shielding effectiveness of iron ore tailings/cement composite, Case Stud. Constr. Mater. 21 (2024) e03740, https://doi.org/10.1016/j.cscm.2024.e03740.
[42] R. Baimanova, F. Luo, M. Yang, Preparation of iron-doped titania nanoparticles and their UV-blue light-shielding capabilities in polyurethane, Materials 15 (20) (2022) 7370, https://doi.org/10.3390/ma15207370.
[43] C. Yu, Y. Meng, B. Yang, F. Sun, G. Yang, Y. Han, X. Li, Iron oxide/CNT-based artificial nacre for electromagnetic interference shielding, Nano Res. 17 (7) (2024) 6560–6566, https://doi.org/10.1007/s12274-024-6567-7.
[44] B.M. Basavaraja Patel, M. Revanasiddappa, D.R. Rangaswamy, S. Manjunatha, Y. T. Ravikiran, Electrical conductivity and EMI shielding studies of iron-decorated polypyrrole-fly ash nanocomposites, Mater. Today Proc. 49 (5) (2022) 2253–2259, https://doi.org/10.1016/j.matpr.2021.09.337.
[45] M. Krajewski, W. Dzwolak, B. Mitura-Nowak, S. Pawłowska, Poly(Vinylidene Fluoride-co-Hexafluoropropylene) films filled with iron nanoparticles for infrared shielding applications, macromol, Rapid Commun 44 (9) (2023) 2300038, https://doi.org/10.1002/marc.202300038.
[46] Z. Ma, J. He, S. Liu, J. Wang, H. Li, W. Zhao, Y. Wu, L. Li, Gradient layered MXene/Fe3O4@CNTs/TOCNF ultrathin nanocomposite paper exhibiting effective electromagnetic shielding and multifunctionality, Nano Res. 17 (9) (2024) 8233–8242, https://doi.org/10.1007/s12274-024-6824-x.
[47] F.I. El-Agawany, K.A. Mahmoud, E. Kavaz, R. El-Mallawany, Y.S. Rammah, Evaluation of nuclear radiation shielding competence for ternary Ge–Sb–S chalcogenide glasses, Appl. Phys. A 126 (4) (2020) 258, https://doi.org/10.1007/s00339-020-3426-7.
[48] A.A.A. Awshah, U.S.A. Aliyu, H.M. Kamari, I.G. Geidam, R. El-Mallawany, A. M. Hamza, S.H. Alazoumi, Polarizability and optical properties of TeO2–ZnO glass system doped with Nd2O3, J. Mater. Sci. Mater. Electron. 33 (17) (2022) 13493–13505, https://doi.org/10.1007/s10854-022-08284-9.
[49] A.S. Abouhaswa, H.M. Zakaly, S.A. Issa, M. Pyshkina, R. El-Mallawany, M. Y. Mostafa, Lead borate glasses and synergistic impact of lanthanum oxide additive: optical and nuclear radiation shielding behaviors, J. Mater. Sci. Mater. Electron. 31 (17) (2020) 14494–14501, https://doi.org/10.1007/s10854-020-04009-y.
[50] D. Li, F. Ling, Z. Zhu, X. Zhang, Theoretical studies on the structural, electronic, and optical properties of Cu2CdGeSe4, Phys. B Condens. Matter 406 (17) (2011) 3299–3302, https://doi.org/10.1016/j.physb.2011.05.021.
[51] X. Xu, Y. Liu, C. Han, X. Sun, Design method of cylindrical self-shielding coils in spindle-shaped magnetic shielding cylinders eliminating ferromagnetic boundary coupling, IEEE Trans. Instrum. Meas. 74 (2025) 9508511, https://doi.org/10.1109/tim.2025.3524787.
[52] C. Xiao, J. Peng, Y. Jiao, Q. Shen, Y. Zhao, F. Zhao, Q. Song, Strong and tough multilayer heterogeneous pyrocarbon-based composites, Adv. Funct. Mater. 34 (51) (2024) 2409881, https://doi.org/10.1002/adfm.202409881.